Skin-Friction and Forced Convection from Rough and Smooth Plates

Aubrey G. Jaffer
e-mail: agj@alum.mit.edu

Abstract

Since the 1930s, theories of skin-friction drag from plates with rough surfaces have been based on an analogy to turbulent flow within pipes having rough interiors. Failure of this analogy at low Reynolds number (Re) flow rates has frustrated attempts to create a comprehensive theory.

By introducing the concept of self-similar roughness, this investigation derives formulas for a plate's skin-friction drag coefficient and forced convection given its characteristic-length, root-mean-squared (RMS) height-of-roughness, and isotropic spatial period. Compared with this novel theory, the RMS relative error of measurements from Pimenta, Moffat, and Kays (1975) is 4.5%; from Bergstrom, Akinlade, and Tachie (2005) wire meshes and perforated plates, it is 3.3% and 4.2%, respectively; from experiments conducted for this investigation, it is 2.1%.

Building on its analysis of self-similar roughness, this investigation also derives a formula for the skin-friction coefficient of a smooth plate; this formula matches measurements from Smith and Walker (1959) and Spalding and Chi (1964) spanning $10^5 \le Re \le 10^9$ with 0.75% RMS relative error. Its new formula for smooth turbulent forced convection is in agreement with Lienhard (2020), while expanding the range to all Prandtl numbers.

This research did not receive any specific grant from funding agencies in the public, commercial, or not-for-profit sectors.

Table of contents

1. **Introduction**

Drag is the pressure opposing fluid flow by an object. Drag consists of "form drag", due to fluid being deflected around the object, and "skin-friction drag" (or "resistance") due to dissipation of the viscous friction stress (shearing stress) generated by flow along the object's surface. Related to skin-friction, "forced convection" is the heat transfer to or from a surface which is induced by fluid flow along that surface. Skin-friction and forced convection are fundamental processes with applications from engineering to geophysics.

Circa 1930, Prandtl [1] and von Kármán [2] developed theories for frictional resistance along (smooth) plates from the results of research on flow through pipes; this is the "pipe-plate analogy".

In 1934, Prandtl and Schlichting [3] developed a theory of skin-friction resistance for rough plates based on their analysis of Nikuradse's [4] measurements of sand glued inside pipes ("sand-roughness"). The conclusion of the (translated) paper states:

> "The resistance law just derived for rough plates has chiefly validity for a very specific type of roughness, namely a smooth surface to which sand grains have been densely attached and where the Nikuradse pipe results have been taken as the basis...
>
> A single roughness parameter (the relative roughness) will in all likelihood no longer answer the purpose in continued investigations of the roughness problem."

In 1936, Schlichting [5] investigated the velocity field and skin-friction of water flowing through a closed rectangular channel having one wall replaced in turn by a series of plates, each having an array of identical protrusions attached: spheres, spherical caps (bumps), or cones. The protrusions were positioned on the plates in a hexagonal array which was elongated 15% in the direction of flow.

There was significant pressure drop between the inflow and outflow of the channel, so it was not a case of the isobaric (no pressure drop) flow which occurs along external plates. The similarity of closed channel flow to pipe flow is well known, but does not support or refute treating rough pipe interiors and plates analogously.

In 1954, Hama [6] described three challenges of the pipe-plate analogy:

> "Now there is no obvious reason why pipe flow and boundary-layer flow should be identical or even similar. First, a pressure gradient is essential for flow through a pipe but not along a plate. Second, pipe flow is confined and perforce uniform, while flow along a plate develops semi-freely and bears no such a priori guarantee of displaying similar velocity profiles at successive sections. Finally, the diameter and roughness size are the only geometrical dimensions of established flow in pipes, whereas at least three linear quantities are necessary to characterize the boundary-layer."

Fluid in contact with the plate surface has 0 velocity. The "boundary-layer" is flow near the surface which has velocity different from the bulk flow (or "free-stream") velocity u.

Hama attempted to confirm the rough pipe-plate analogy with measurements of wire screens affixed to smooth plates, but concluded that it was confirmed only in the fully rough regime (defined below).

Roughness in prior works [3, 4, 5, 6, 7, 8, 9, 10, 11] is reported as sand-roughness k_S, the height of "coarse and tightly placed roughness elements such as, for example, coarse sand grains glued on the surface" [9].

Testing a machined analogue of sand-roughness, Pimenta, Moffat, and Kays [7] wrote in 1975 that, while the agreement of their data with the Prandtl-Schlichting plate model was "rather good" in the fully rough regime, their apparatus did not have the same behavior as "Nikuradse's sand-grain pipe flows in the transition region."

By modeling the wake component of the velocity profile, in 1985 Mills and Hang [8] presented a formula improving the match with Pimenta et al data in the rough regime, but was silent about other flow regimes.

Along with laminar flow, the theory for flow within pipes (and channels) distinguishes three turbulent flow regimes: smooth, (fully) rough, and transitional. Smooth turbulent pipe flow encounters viscous resistance which varies inversely with the fluid velocity per viscosity ratio. Rough pipe flow encounters resistance which varies with the height-of-roughness, while the effect of viscosity is negligible. The transitional regime describes the range of flow rates where both viscosity and roughness affect the resistance (Colebrook [12]).

The Reynolds number (Re) represents the bulk fluid flow rate (far from the plate); Reynolds numbers with subscripts represent other flow rates. The local Reynolds number $Re_x = x\,Re/L$, where x is the distance from the leading edge of the plate in the direction of flow, and characteristic-length L is the length scale for the physical system. Except where stated otherwise in this investigation, L is plate length in the direction of flow.

Drag in prior works is represented by the local drag coefficient c_f or C_f, which is a function of relative sand-roughness x/k_S, and of the Reynolds number or a subscripted Reynolds number.

Prandtl and Schlichting [3] specified the boundaries between flow regimes using the "sand-roughness Reynolds number" Re_k. For plates, they assigned the boundaries between smooth, transitional, and rough regimes at $Re_k = 7.08$ and 70.8. Pimenta et al [7] gave $Re_k = 65$ as the transitional-to-rough boundary.

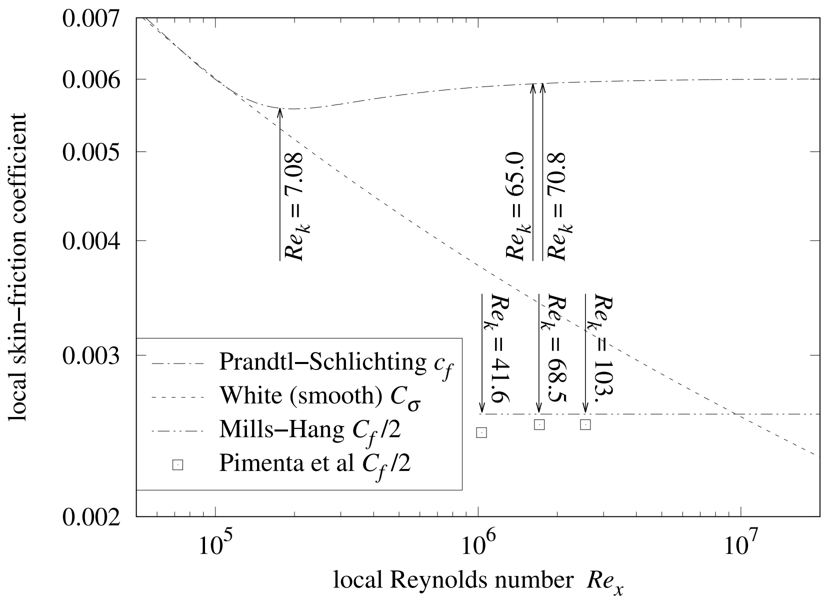

Figure 1 local c_f versus Re_x

Figure 1 presents skin-friction coefficient curves, Re_k regime boundaries and values, and measurements from a plate having relative sand-roughness $L/k_S = 1200$.

In pipes, the resistance of rough flow is never less than the resistance of smooth turbulent flow occurring in otherwise identical conditions. A tenet of the rough pipe-plate analogy is that this rule also applies to rough, external plates; for example, the "Prandtl-Schlichting c_f" curve is never less than the "White (smooth) C_σ" curve in Figure 1.

The Pimenta et al measurements are much closer to $c_f/2$ than they are to c_f.[1] Pimenta et al [7] and Mills and Hang [8] both referred to skin-friction coefficients as $C_f/2$. All three measurements in Figure 1 are less than the smooth turbulent coefficient C_σ. Thus, these measurements can not be in any turbulent flow regime; the remaining alternative is laminar flow. Laminar flow coefficients have a steeper slope than C_σ; yet these measurements are nearly at the constant level predicted by Mills-Hang $C_f/2$ for the rough regime.

This is where the pipe-plate analogy fails for roughness. Rough turbulent skin-friction coefficients can take values less than smooth turbulent coefficients for external plates, but not inside pipes.

Nevertheless, research continued based on the pipe-plate analogy. A 2004 survey article by Jiménez [13] voiced the enduring faith in the rough pipe-plate analogy: "The theoretical arguments are sound, but the experimental evidence is inconclusive."

[1] The Bergstrom, Akinlade, and Tachie [14] local friction coefficient (C_f) measurements of woven wire meshes and perforated sheets (Sections 21 and 22 of the present work) are also much closer to Prandtl-Schlichting $c_f/2$ than they are to c_f.

In 2001, Tachie, Bergstrom, Balachandar, and Ramachandran [15] combined multiple studies to propose a correlation for skin-friction coefficient as a function of the momentum-thickness Reynolds number Re_θ:

$$\begin{aligned} C_f(Re_\theta) = \big[&4.13\times10^{-2} - 2.68\times10^{-2}\,\log_{10} Re_\theta + 6.528\times10^{-3}\,\log_{10}^2 Re_\theta \\ &- 5.54\times10^{-4}\,\log_{10}^3 Re_\theta\big] \pm 7\% \qquad 150 < Re_\theta < 15000 \end{aligned} \tag{1}$$

As a function of a roughness metric, formula (1) has no predictive value because Re_θ must be computed from velocity field measurements along the surface in question.

Circa 2005, Bergstrom, Akinlade, and Tachie [14], performed experiments with sandpapers, woven wire meshes, and perforated sheets attached onto a flat plate, reporting that:

$$\sqrt{C_f} = [0.360 \pm 0.025]\,\frac{\delta^*}{\delta} \tag{2}$$

where δ^* is the displacement thickness and δ is the 99% velocity boundary-layer thickness. As a function of a roughness metric, formula (2) also has no predictive value because both δ^* and δ must be computed from velocity field measurements along the surface in question. Fortunately, they included free-stream velocity in their tables, allowing comparisons of their skin-friction data with the present theory.

Lastly, an additional complication was described by S. F. Hoerner in the discussion section of Hama [6]:

> "One conclusion from sand experiments has been the expectation that from then on every rough surface should have a constant terminal drag coefficient. As early as 1924, it has been demonstrated (by Hopf and Fromm in *Zeitschr. Angew. Math. Mech.*, 1923:329-339) that certain types of roughness do not show any constant coefficients."

The sand-roughness metric's lack of generality, the need for additional roughness parameters, non-constant terminal drag coefficients, and the failure of the pipe-plate analogy for roughness motivate a fresh theoretical analysis of isobaric flow along a rough plate which is based on a traceable roughness metric.

2. Roughness metrics

Two established, traceable roughness metrics are the root-mean-squared (RMS) height-of-roughness and the arithmetic-mean height-of-roughness. For an elevation function $z(x,y)$ defined on area A having a convex perimeter, its mean elevation $\overline{z}$ and RMS height-of-roughness ε are:

$$\overline{z} = \int_A z\,\mathrm{d}A \Big/ \int_A \mathrm{d}A \qquad \varepsilon = \sqrt{\int_A |z-\overline{z}|^2\,\mathrm{d}A \Big/ \int_A \mathrm{d}A} \tag{3}$$

The arithmetic-mean height-of-roughness is defined in terms of the same mean elevation $\overline{z}$:

$$\int_A |z-\overline{z}|\,\mathrm{d}A \Big/ \int_A \mathrm{d}A \tag{4}$$

Modeling sand-roughness grains as diameter k_S spheres sitting in a pool of depth g glue, the mean elevation $\overline{z}$ of a cell of area A containing one sphere is:

$$\overline{z} = \int_0^{k_S/2} \frac{2\,\pi\,x}{A}\left[\sqrt{\frac{k_S^2}{4}-x^2}+\frac{k_S}{2}\right]\mathrm{d}x + \left[A - \frac{\pi\,k_S^2}{4}\right]\frac{g}{A} = g + \frac{5\,\pi\,k_S^3}{24\,A} - \frac{\pi\,k_S^2\,g}{4\,A} \tag{5}$$

From formula (3), its RMS height-of-roughness ε is:

$$\varepsilon = \sqrt{\int_0^{k_S/2} \frac{2\,\pi\,x}{A}\left|\sqrt{\frac{k_S^2}{4}-x^2}+\frac{k_S}{2}-\overline{z}\right|^2 \mathrm{d}x + \left[1 - \frac{\pi\,k_S^2}{4\,A}\right]|g-\overline{z}|^2} \tag{6}$$

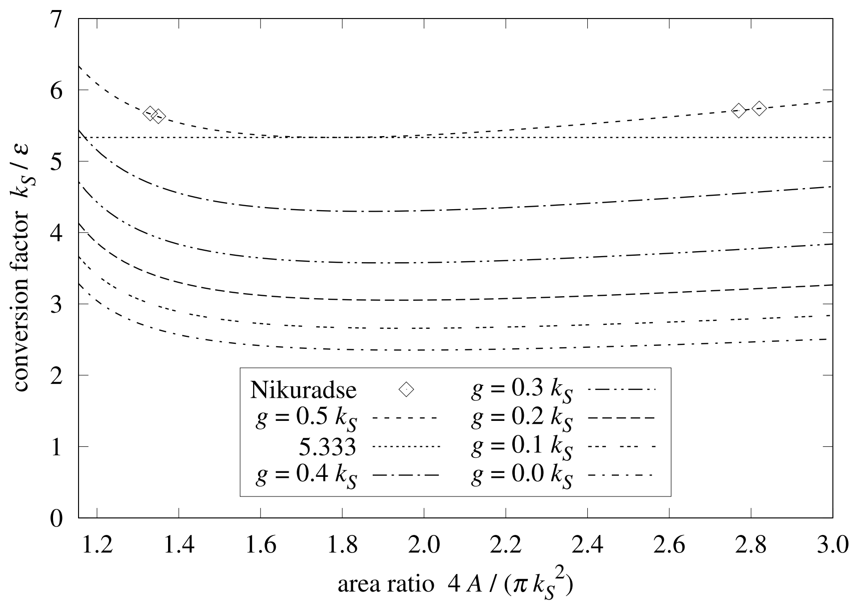

Figure 2 k_S/ε versus cell area of sand-roughness

Figure 2 shows k_S/ε versus the cell per shadow area ratio, at six glue-levels between 0% and 50% of k_S. Table 1 lists k_S, grain densities, and conversion factors for Nikuradse's [4] sand coatings, assuming $g = 0.5\,k_S$.

k_S	grains/cm^2	k_S/ε @ $g = 0.5\,k_S$
.08 cm	150	5.67
.04 cm	590	5.63
.02 cm	1130	5.74
.01 cm	4600	5.71

Table 1 Nikuradse's sand coatings

Afzal, Seena, and Bushra [16] fit 5.333 as the RMS to sand-roughness conversion factor k_S/ε, and 6.45 as the arithmetic-mean to sand-roughness conversion factor in pipes. $k_S/\varepsilon = 5.333$ is a broad minimum of the $g = 0.5\,k_S$ curve in Figure 2.

The "k_S/ε @ $g = 0.5\,k_S$" column values in Table 1 ("Nikuradse" in Figure 2) match each other within 2%. The tightest spread on Table 1 data with the arithmetic-mean height-of-roughness exceeds 20%. Thus, sand-roughness correlates an order of magnitude more strongly with RMS height-of-roughness than with arithmetic-mean height-of-roughness.

Flack, Schultz, Barros, and Kim [17] measured skin-friction from grit-blasted surfaces in a duct, writing "The root-mean-square roughness height is shown to be most strongly correlated with the equivalent sand-roughness height (k_S) for the grit-blasted surfaces."

Arithmetic-mean height-of-roughness will not be considered further by this investigation.

The plate tested by Pimenta et al [7] was composed of 11 layers of densely packed 1.27 mm diameter metal spheres "arranged such that the surface has a regular array of hemispherical roughness elements." Having been brazed together, there was no pool of glue surrounding the spheres. Shrinking the cell to the sphere's shadow, $\pi\,k_S^2/4$, the RMS height-of-roughness of the top half of the 1.27 mm sphere is 0.150 mm. Converting $k_S = 0.794\,\mathrm{mm}$ from Pimenta et al by the 5.333 conversion factor from Afzal et al [16] yields $k_S/5.333 \approx 0.149\,\mathrm{mm}$, which matches 0.150 mm within 1%.

3. Formulas from prior works

In *Boundary-layer theory* [9], Prandtl and Schlichting gave formulas for fully rough local (c_f) and plate average ($\overline{c_f}$) skin-friction coefficient for a rough plate as a function of x/k_S and L/k_S, respectively.

$$c_f = \left[2.87 + 1.58 \log_{10} \frac{x}{k_S}\right]^{-2.5} \qquad x \le L \tag{7}$$

$$\overline{c_f} = \left[1.89 + 1.62 \log_{10} \frac{L}{k_S}\right]^{-2.5} \qquad 10^2 < \frac{L}{k_S} < 10^6 \tag{8}$$

Mills and Hang [8] gave a formula (9) which is more accurate than formula (7) on the local skin-friction measurements from Pimenta et al [7]. Their local (C_f) and average ($\overline{C_f}$) coefficient formulas were:

$$C_f = \left[3.476 + 0.707 \ln \frac{x}{k_S}\right]^{-2.46} \qquad 750 < \frac{x}{k_S} < 2750 \tag{9}$$

$$\overline{C_f} = \left[2.635 + 0.618 \ln \frac{L}{k_S}\right]^{-2.57} \tag{10}$$

White [10] gave formula (11) for fully rough local skin-friction coefficient:

$$C_f = \left[1.4 + 3.7 \log_{10} \frac{x}{k_S}\right]^{-2} \qquad \frac{x}{k_S} > \frac{Re_x}{1000} \tag{11}$$

White is also the source of a widely used formula for turbulent skin-friction coefficient for smooth plates:

$$C_\sigma(Re_x) = \frac{0.455}{\ln^2(0.06\, Re_x)} \tag{12}$$

Mills and Hang [8] derived the average formula (10) from the local formula (9) by fitting a curve to the result of the numerical integration in formula (13):

$$\overline{C_f}\left(\frac{L}{k_S}\right) = \frac{k_S}{L - L_0} \int_{L_0/k_S}^{L/k_S} C_f(x)\, \mathrm{d}x \tag{13}$$

The local formulas (7), (9), and (11) each have a singularity where the expression containing the logarithm is 0. The lower limit of integration (L_0/k_S) must be large enough to avoid this; but the lower limit is not revealed in the prior works. The averaging formula (13) is quite sensitive to the lower limit because the largest value of the local formula occurs there.

For the Mills-Hang formula (9), with lower bound $L_0/k_S = 1.6$ and initial $\mathrm{d}x/k_S = 0.01$, integration of the local C_f is within $\pm 0.5\%$ of the average $\overline{C_f}$ in formula (10) over the range $200 < x/k_S < 200 \times 10^3$.

For the Prandtl-Schlichting formula (7), with lower bound $L_0/k_S = 0.5$ and initial $\mathrm{d}x/k_S = 0.5$, integration of the local c_f is within $\pm 0.5\%$ of the average $\overline{c_f}$ in formula (8) over the range $200 < x/k_S < 200 \times 10^3$.

Churchill [11] compared 8 formulas from various sources with the data from Pimenta et al [7]; it did not find any to be significantly closer to the measurements than the Mills-Hang local formula (9).

Churchill had distinct formulas for computing the average (mean) skin-friction C_m from local C_f for smooth and rough surfaces, respectively:

$$C_m = C_f \frac{1 - 4.516\sqrt{C_f}}{1 - 7.965\sqrt{C_f} + 21.52\, C_f} \tag{14}$$

$$C_m = C_f \frac{1 - 4.516\sqrt{C_f}}{1 - 7.965\sqrt{C_f}} \tag{15}$$

Fully rough regime formulas are compared in Section 19.

4. **Rough turbulence**

Forced flow along a plate with a rough surface differs in character from forced flow along a smooth surface because roughness disrupts what would otherwise be a viscous sub-layer adjacent to the plate. Lienhard and Lienhard [18] teaches: "Even a small wall roughness can disrupt this thin sublayer, causing a large decrease in the thermal resistance (but also a large increase in the wall shear stress)."

Jiménez [13] wrote "In flows with $\delta/k < 50$, the effect of the roughness extends across the boundary-layer, and is also variable. There is little left of the original wall-flow dynamics in these flows, which can perhaps be better described as flows over obstacles."

This investigation focuses initially on the case where flow over obstacles dominates the dynamics. It does this by modeling the rough shearing stress as resulting from the interaction of flow with a roughness which disrupts flow at a succession of scales from L converging to 0. While simpler surfaces may also produce rough turbulence, a roughness which disrupts at this succession of scales surely will. Self-similarity, expressed as a recurrence formula, will be used to succinctly describe such a roughness across scales.

The turbulent boundary-layer thickness along a smooth plate increases proportionally to $x^{4/5}$, where x is the distance from its leading edge (Schlichting [9]). Roughness whose envelope height increases linearly with x can disrupt emerging boundary-layers repeatedly along the entire plate.

This approach departs from prior works because their continuous boundary-layer assumption is incompatible with roughness-as-disruption.

5. **Profile roughness**

Simpler than surface roughness, roughness profiles can nonetheless be informative.

Let a "profile roughness" be a function $z(x)$ with $0 \le x \le L$. Given a roughness profile $z(x)$, its mean elevation $\overline{z}$ and RMS height-of-roughness ϵ are computed similarly to surface roughness ε:

$$\overline{z} = \frac{1}{L}\int_0^L z(x)\,\mathrm{d}x \qquad \epsilon = \sqrt{\frac{1}{L}\int_0^L |z(x)-\overline{z}|^2\,\mathrm{d}x} \tag{16}$$

Let a "self-similar profile roughness" be a profile roughness function $z(x)$ with (integer) branching factor $n \ge 2$ such that the RMS height-of-roughness of $z(x)$ over an interval $x_0 < x < x_n$ is n times the RMS height-of-roughness of $z(x)$ over each equally divided sub-interval $x_t < x < x_{t+1}$ with $0 \le t < n$ at a succession of scales converging to 0.

The x intervals are open; each $z(x_t)$ value contributes to the height-of-roughness of its parent interval, but not to any sub-interval.

A consequence of this definition is that the ratio of the length of an interval per the RMS height-of-roughness of z over that open interval will be invariant through its succession of scales.

Of particular interest are self-similar roughness profiles which are permutations of the linear ramp $z(x) = \varsigma\, x/L$ with $0 \le x \le L$. Every elevation from 0 to peak height ς occurs exactly once in a ramp-permutation.

The only occurrence of x in formula (16) is $z(x)$; hence the RMS height-of-roughness calculation depends only on the z values, not on their relation to x. Thus, the height-of-roughness of any ramp-permutation is identical to the height-of-roughness of the linear ramp:

$$\epsilon = \sqrt{\frac{1}{L}\int_0^L \left|\frac{\varsigma\, x}{L} - \frac{\varsigma}{2}\right|^2 \mathrm{d}x} = \frac{\varsigma}{\sqrt{12}} \tag{17}$$

6. Self-similar ramp permutations

A self-similar integer sequence $Y(t,w)$ from integers $0 \le t < w = n^q$ allows self-similar behavior to be explored with a finite approximation. Letting $t = \lfloor w\,x/L \rfloor \equiv \text{floor}(w\,x/L)$ constructs a roughness profile from a sequence by $z(x) = [\varsigma/w]\,Y(\lfloor w\,x/L \rfloor, w)$. These three examples are $n = 2$ ramp-permutation sequences:

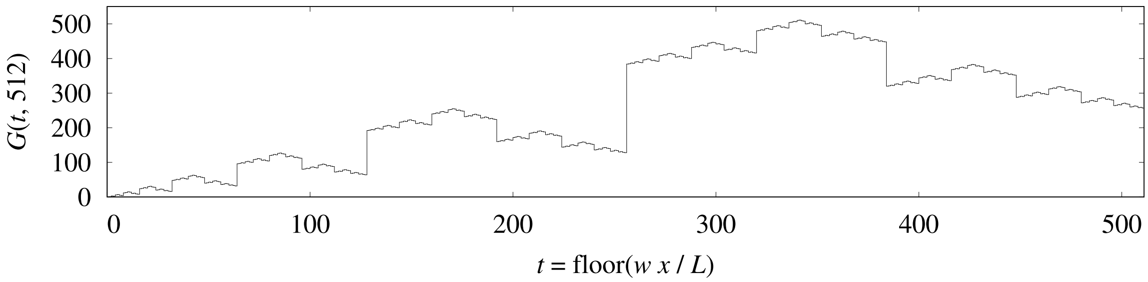

Figure 3 Gray-code profile roughness

Self-similar recurrence (18) defines the integer Gray-code sequence $G(t,w)$ shown in Figure 3.

$$G(t,w) = \begin{cases} t, & \text{if } w = 1; \\ w + G(w - 1 - [t \bmod w], w/2), & \text{if } \lfloor t/w \rfloor = 1; \\ G(t \bmod w, w/2), & \text{otherwise.} \end{cases} \tag{18}$$

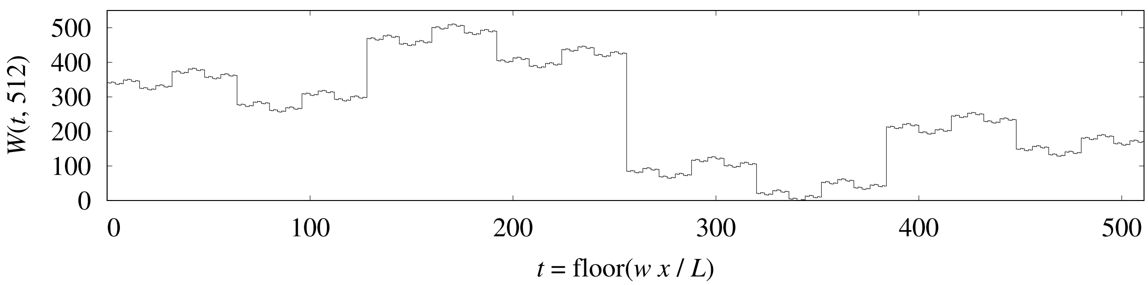

Figure 4 wiggliest self-similar profile roughness

Recurrence (19) defines the integer sequence $W(t,w)$ shown in Figure 4; it reverses direction at each bifurcation, yielding a wiggliest possible self-similar $n = 2$ ramp-permutation sequence.

$$W(t,w) = \begin{cases} t, & \text{if } w = 1; \\ \lfloor t/w \rfloor w + W(w - 1 - [t \bmod w], w/2), & \text{otherwise.} \end{cases} \tag{19}$$

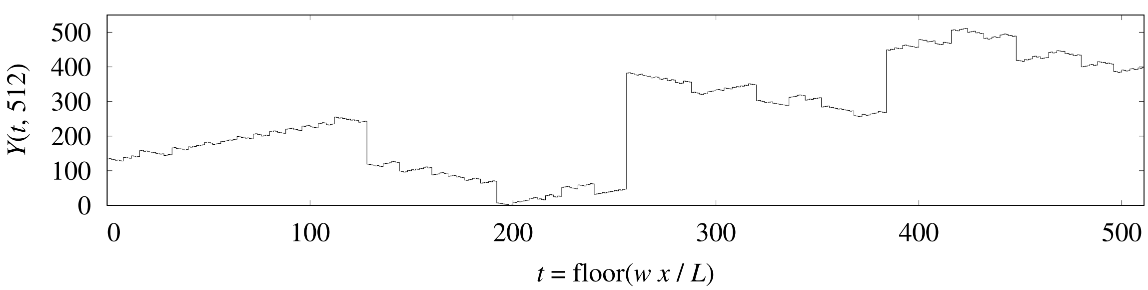

Figure 5 random reversal bifurcation profile roughness

Figure 5 shows a sequence generated by randomly reversing or not at each bifurcation in recurrence (20).

$$Y(t,w) = \begin{cases} t, & \text{if } w = 1; \\ w + Y(w - 1 - [t \bmod w], w/2), & \text{with probability 0.5;} \\ Y(t \bmod w, w/2), & \text{otherwise.} \end{cases} \tag{20}$$

For a given $w = 2^q \ge 4$, there are 2^{w-1} distinct self-similar $n = 2$ ramp-permutation sequences, but only 2 distinct ramps and 2 distinct wiggliest sequences.

7. Friction travel and velocity

In the conversion of bulk flow to rough turbulence, some particles of fluid must move in directions not parallel to the bulk flow. Such movement results from deflections of flow by roughness peaks, pits, ridges, and valleys; the amount of turbulence induced by a roughness should grow as the height-of-roughness increases.

Let "run" be the horizontal axis and "friction" be the vertical axis of a profile roughness such as in Figure 5. For an integer ramp-permutation sequence $Y(t,w)$, the sum of the (dimensionless) lengths of all run segments is $w-1=2^q-1$. The sum of the friction segment lengths is:

$$\sum_{t=0}^{2^q-2} |Y(t,2^q)-Y(t+1,2^q)| \tag{21}$$

If a particle of fluid traces the ramp-permutation sequence $Y(t,w)$ between $t=0$ and $t=w-1$, then $w-1$ is the run distance it travels, while formula (21) is the friction distance.

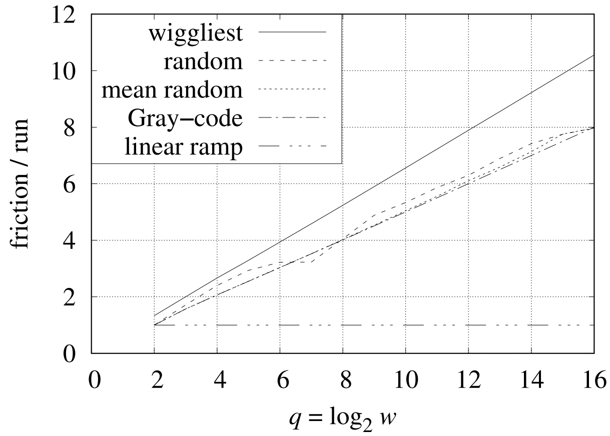

Figure 6 travel along profile roughness

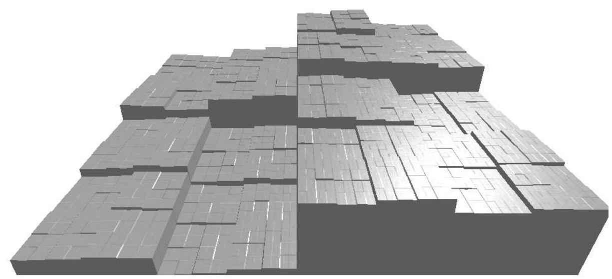

Figure 7 random reversal ramp surface

Figure 6 shows the friction travel per run travel ratio versus q, the (integer) base-2 logarithm of w. The linear ramp's slope is 0; the Gray-code's is 1/2; the random reversal cases are approximately 1/2; and the wiggliest roughness has slope 2/3.

A wiggliest roughness sequence $W(t,w)$ is an extreme case; it reverses friction direction at each increment of run (t). For each wiggliest roughness sequence with $w \geq 4$ there are $2^{w-1}-2$ other random reversal roughness sequences. The linear ramp never reverses direction. For each linear ramp sequence there are $2^{w-1}-2$ other random reversal sequences. Being outliers, $W(t,w)$ and linear ramps are excluded from further consideration as roughness.

In Figure 6, the friction per run ratios for Gray-code and random reversal sequences are close to:

$$\frac{q}{2} \equiv \frac{\log_2 w}{2} \tag{22}$$

$Y(t,w)$, t, and w are dimensionless. The friction per run ratio (22) needs to be reformulated in terms of the height-of-roughness. Turning to dimensional analysis, the argument to $\log_2$ must be dimensionless, involve ϵ, and be greater than 1, so that the logarithm will be positive. This friction per run ratio must increase with increasing ϵ; thus, ϵ and the logarithm will be in denominators, yielding:

$$\frac{2}{\log_2(L/\epsilon)} \tag{23}$$

Scaling formula (23) by $1/\sqrt{12}$ from formula (17) converts formula (23) into the RMS friction travel per run travel ratio:

$$\frac{1}{\sqrt{12}}\,\frac{2}{\log_2(L/\epsilon)} = \frac{1}{\sqrt{3}\,\log_2(L/\epsilon)} \tag{24}$$

Considering the run travel and friction travel with respect to time lets formula (24) also serve as the friction velocity u_τ per bulk flow velocity u ratio.

8. **Skin-friction from a rough plate**

Newberry and Savage [19] demonstrated that some self-similar systems which are modeled using continuous power-law probability distributions can be modeled using discrete power-law distributions.

This investigation uses that idea in reverse. The conversion of run velocity into friction velocity by contact with discrete self-similar $n = 2$ roughness was modeled by formula (24); the u_τ/u conversion ratio for a random self-similar roughness will be inferred using a continuous random variable $Z > 1$ having a Pareto distribution whose frequency of Z is Z^{-2}:

$$\frac{u_\tau}{u} = 1 \Big/ \left[\sqrt{3}\int_\varepsilon^L \frac{Z}{Z^2}\,\mathrm{d}Z\right] = \frac{1}{\sqrt{3}\,\ln(L/\varepsilon)} \tag{25}$$

In the generalization of formula (24) to random self-similar roughness in formula (25), the profile height-of-roughness ϵ was replaced by the surface height-of-roughness ε. As with the profile RMS height-of-roughness, the surface RMS height-of-roughness of any permutation of the linear ramp from 0 to ς is $\varsigma/\sqrt{12}$. Thus, the $1/\sqrt{3}$ $(= 2/\sqrt{12})$ coefficient is the same in formulas (24) and (25)

An example of self-similar ramp-permutation surface roughness is shown in Figure 7.

A plate surface composed of parallel, edge-to-edge ridges and valleys will disrupt flow which is perpendicular to the ridges, but may not disrupt flow which is parallel to the ridges. To avoid this complication, this investigation considers only surface roughness which is "isotropic": rotating the flow azimuth in the plane of the rough surface does not substantially affect its behavior.[2]

The skin-friction coefficient $\overline{f_c}$ is the ratio of the shearing stress τ_2 per the fluid flow's dynamic pressure (kinetic energy density) $\rho\, u^2/2$, where ρ is the fluid density:

$$\overline{f_c} = \frac{\tau_2}{\rho\, u^2/2} \tag{26}$$

Both τ_2 and $\rho\, u^2/2$ have units of pressure, $\mathrm{kg}/(\mathrm{m}\cdot\mathrm{s}^2)$; hence $\overline{f_c}$ is dimensionless. Multiplication by formula (25) converts bulk flow velocity u into friction velocity u_τ, from which τ_2 is derived:

$$u_\tau = \frac{u}{\sqrt{3}\,\ln(L/\varepsilon)} \qquad \tau_2 = \frac{\rho\, {u_\tau}^2}{2} = \frac{\rho\, u^2}{6\,\ln^2(L/\varepsilon)} \qquad \frac{L}{\varepsilon} \gg 1 \tag{27}$$

Combining equations (26, 27) yields the average skin-friction coefficient of an isotropic, self-similar rough surface:

$$\overline{f_\rho} = \frac{1}{3\,\ln^2(L/\varepsilon)} \qquad \frac{L}{\varepsilon} \gg 1 \tag{28}$$

Prandtl and Schlichting [3] calculated $\tau = \rho\, {u_\tau}^2$, not $\tau_2 = \rho\, {u_\tau}^2/2$. As a result, $\overline{c_f} > 2\,\overline{f_\rho}$ and $c_f > 2\, f_\rho$. Both Pimenta et al [7] and Mills and Hang [8] treat $c_f/2$ as the skin-friction coefficient.

Equation (28) is compared with measurements in Sections 19, 21, and 22.

9. **Skin-friction from a smooth plate**

For a given $Re \gg 1$ there must be an L/ε ratio so large that an L length plate with self-similar roughness ε has turbulence-inducing behavior midway between that of a rough surface and that of a smooth surface.

Let the "roughness Reynolds number" Re_ε derive from friction velocity u_τ at scale ε:

$$Re_\varepsilon = \frac{u_\tau\, \varepsilon}{\nu} = \frac{u}{\sqrt{3}\,\ln(L/\varepsilon)}\,\frac{\varepsilon}{\nu} = \frac{Re}{\sqrt{3}\,[L/\varepsilon]\,\ln(L/\varepsilon)} \tag{29}$$

where ν is the fluid kinematic viscosity and $Re = L\, u/\nu$. The Re strength at which rough plate skin-friction transitions to smooth plate skin-friction will have the same Re_ε value at all $L/\varepsilon \gg 1$. Combining $Re_\varepsilon = 1$ with formula (29) relates Re with L/ε at this transition:

$$Re = \sqrt{3}\,\frac{L}{\varepsilon}\,\ln\frac{L}{\varepsilon} \tag{30}$$

[2] This constraint is quantified in Section 11.

Relation (30) linking Re with L/ε suggests that the smooth turbulent friction coefficient $\overline{f_\sigma}$ can be inferred from formulas (28, 30). However, there being no roughness on a smooth plate, $\overline{f_\rho}$ formula (28) must be adapted for this application. Scaling $\overline{f_\rho}(L/\varepsilon)$ by $\sqrt[3]{2}$, and its argument by $1/\mathrm{e}$:

$$\overline{f_\sigma} = \sqrt[3]{2}\;\overline{f_\rho}\left(\frac{L}{\mathrm{e}\,\varepsilon}\right) = \sqrt[3]{2}\left[\frac{1}{3}\ln^{-2}\frac{L}{\mathrm{e}\,\varepsilon}\right] \tag{31}$$

L/ε can be eliminated from formulas (30, 31) using the Lambert W function, the inverse of $\varphi\exp\varphi$. The inverse of a related form, $\vartheta = \varphi\ln\varphi$, is $\varphi = \exp \mathrm{W}_0(\vartheta)$, where W_0 is the principal branch of W.

$$\overline{f_\sigma} = \frac{\sqrt[3]{2}}{3}\ln^{-2}\left(\frac{\exp\left(\mathrm{W}_0\left(Re/\sqrt{3}\right)\right)}{\mathrm{e}}\right) = \frac{\sqrt[3]{2}/3}{\left[\mathrm{W}_0\left(Re/\sqrt{3}\right)-1\right]^2} \qquad Re \gg \sqrt{3}\,\mathrm{e} \tag{32}$$

The coefficient $\sqrt[3]{2}/3 \approx 0.4200$. Euler's number $\mathrm{e} = \exp(1)$ is a fixed point of $\varphi\ln\varphi$ and its inverse, $\exp(\mathrm{W}_0(\vartheta))$. $Re \gg \sqrt{3}\,\mathrm{e} \approx 4.71$ suggests smooth turbulence's Re lower-bound may be between 20 and 90.

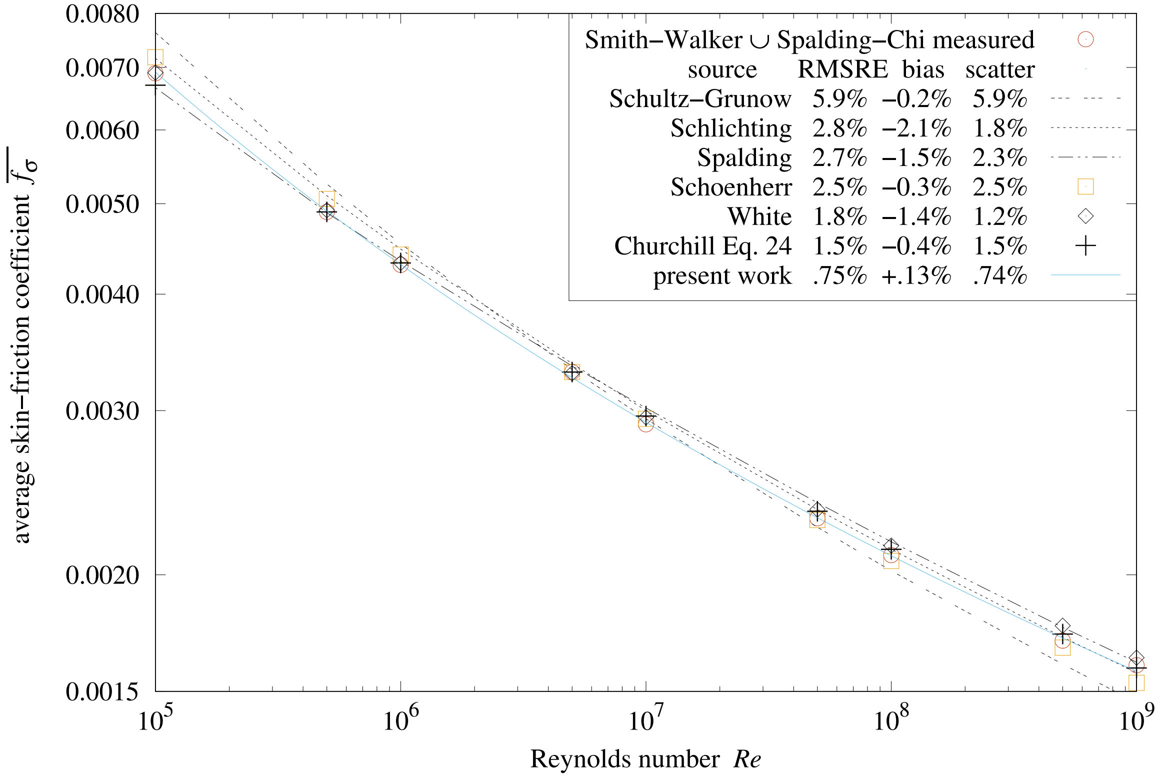

Figure 8 average $\overline{f_\sigma}$ versus Re of smooth plate

Churchill [11] compared smooth turbulent skin-friction coefficient formulas from multiple sources with measurements from Smith and Walker [20], and Spalding and Chi [21]. Figure 8 plots average (not local) coefficient formulas from Churchill; the key gives the RMS error of the measurements relative to each formula.

RMS relative error (RMSRE) gauges the fit of measurements $g(Re)$ to a formula $f(Re)$, with each sample having equal weight. The RMS error of $g(Re)$ relative to $f(Re)$ at n points Re_j is:

$$\sqrt{\frac{1}{n}\sum_{j=1}^{n}\left|\frac{g(Re_j)}{f(Re_j)}-1\right|^2} \tag{33}$$

Figure 8's key splits RMSRE into bias and scatter. The root-sum-squared of bias and scatter is RMSRE. 0.75% RMSRE versus "present work" formula (32) is less error than any formula evaluated by Churchill.

10. **Spectral roughness**

Several prior works [4, 5, 6, 8, 12] use the term "uniform roughness" to describe sand-roughness, implying that its height-of-roughness is the same at all scales. This concept of uniform roughness is incompatible with self-similarity; the RMS height-of-roughness of a portion of a self-similar surface must shrink with the succession of scales converging to 0.

Sand-roughness could be described as "repeated roughness". However, a roughness composed of parallel rows of 1000 sand grains spanning its length can also be described as having 500 sand grain pairs. An unambiguous method for determining the spatial period is needed.

The discrete Fourier transform converts a series of equally-spaced samples of a (roughness) function into complex coefficients for each of its harmonic sinusoidal components. There is a profound connection between the discrete Fourier transform X_j of a roughness sequence $Y(t,w)$ and its RMS height-of-roughness ϵ:

$$X_j = \sum_{t=0}^{w-1} Y(t,w)\, \exp\left(\frac{-2\,\pi\,\mathrm{i}\,j\,t}{w}\right) \qquad \epsilon = \sqrt{\frac{1}{w}\sum_{j=1}^{w-1} |X_j|^2} \tag{34}$$

$|X_{w-j}| = |X_j|$ because all the $Y(t,w)$ elevations have imaginary parts $= 0$; hence there are $w/2+1$ distinct $|X_j|$; only $0 \le j \le w/2$ needs to be considered in the developments which follow.

Constant term $X_0 = \overline{z}$, the mean value of Y, is the only X_j term not included in the sum for ϵ. Because ϵ does not depend on X_0, with $0 < j \le w/2$, the X_j with the largest amplitude is the dominant component of roughness. Let the "period index" j_P be the index j of this X_j having the largest amplitude $|X_j|$.

When one $|X_j|$ is dominant, j_P is well-defined and the roughness profile's spatial period is $L_P = L/j_P$.

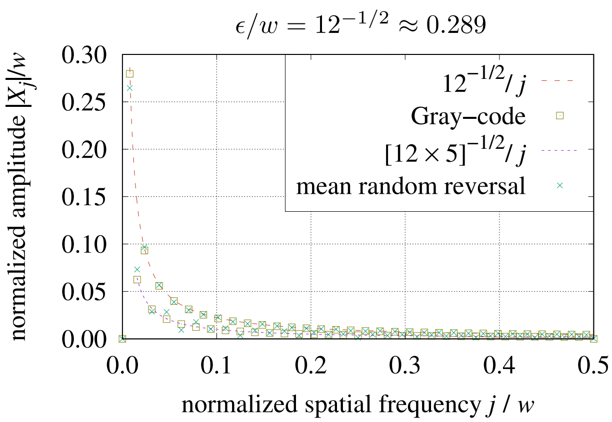

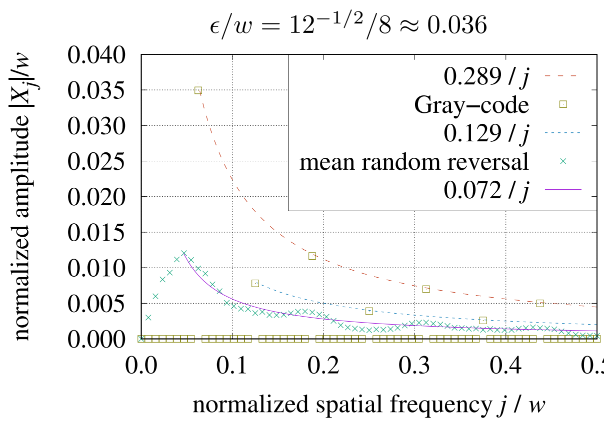

Figure 9 Gray and random spectra **Figure 10 Gray and random eighths**

Figure 9 shows the $|X_j|/w$ amplitude spectrum of the Gray-code roughness profile from Figure 3; also the mean Fourier spectrum amplitudes from 187 instances of 128-point random reversal profiles ($w = 128$). For both spectra, X_1 has the largest amplitude; thus $j_P = 1$, indicating that neither spectrum is from repeated roughness.

Figure 10 shows the spectrum of eight concatenated repetitions of a Gray-code sequence, and the mean Fourier spectrum amplitudes from 187 instances of eight concatenated random reversal sequences. The period index j_P of the Gray-code eighths is 8, as expected; but the random reversal sequences have $j_P = 6$ because their amplitudes are not correlated between the random eighths.

Use of the discrete Fourier transform seems appropriate for detecting and quantifying the spatial period of profile roughness. The next section generalizes this spatial period metric to isotropic surface roughness.

11. Periodic roughness

Let a "periodic roughness" be a flat surface tiled with many isotropic, uniformly sized patches, all sharing the same mean elevation $\overline{z}$ and the same RMS height-of-roughness ε. The mean elevation and RMS height-of-roughness of the surface as a whole will also be $\overline{z}$ and ε, respectively.

Let $S_{s,t}$ be a $w \times w$ matrix of mean elevations from a $w \times w$ square tiling of an $L_w \times L_w$ region of a rough surface. Its 2-dimensional discrete spatial Fourier transform is:

$$X_{j,k} = \sum_{t=0}^{w-1} \sum_{s=0}^{w-1} S_{s,t} \, \exp\left(-2\,\pi\,\mathrm{i}\, \frac{j\,t + k\,s}{w} \right) \tag{35}$$

Let the 2-dimensional period index $j_P = \sqrt{j^2 + k^2} > 0$, where $0 \le j \le w/2$ and $0 \le k \le w/2$ are the indexes of the coefficient $X_{j,k}$ having the largest amplitude, excluding $X_{0,0}$.

The 2-dimensional spatial period $L_P = L_w / j_P$.

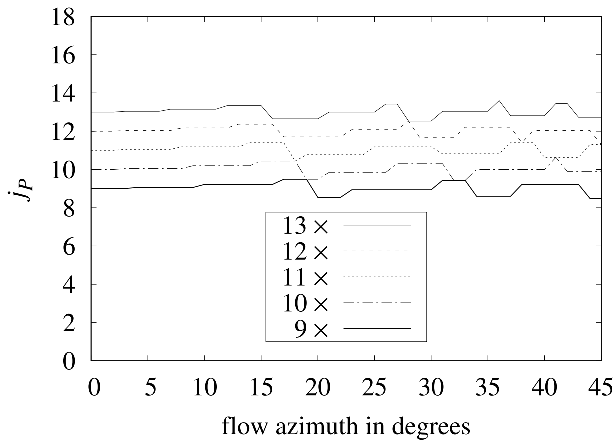

Figure 11 bi-level plate 50%

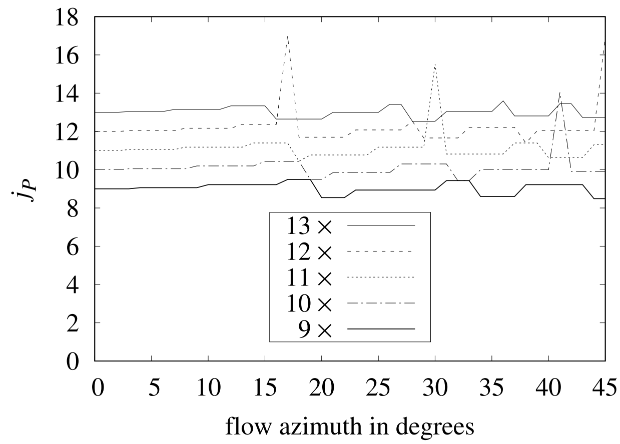

Figure 12 bi-level plate 25%

Figure 11 shows the j_P values for a square equal-area bi-level surface (regular array of square posts on a flat plate) computing $X_{j,k}$ from a 64×64 interpolated sampling of that surface with azimuth from 0° through 45°, and which is scaled between 9 and 13 cells on a side. At each scale, j_P varies within a ± 1 range versus the azimuth. Figure 12 shows a 25% high, 75% low, bi-level surface; some of its j_P traces have peaks outside of the ± 1 range. This suggests a quantitative criterion for surface roughness isotropy:

A surface roughness is isotropic if j_P varies no more than ± 2 through its full rotation.

More specifically, using $w \times w$ ($w \ge 64$) samplings of roughness at nine scales over a 2:1 range such that most of the calculated j_P values satisfy $8 \le j_P \le 16$ at each scale, do 56 sampling trials with randomized offset and randomized azimuth rotation per scale. A roughness is considered isotropic if no more than 5 of the $504 (= 56 \times 9)$ trials have j_P varying more than $\pm w/32$ from its scale.

Using this criterion, square post arrays having an upper area fraction between 27% and 76% are isotropic. Square arrays of circular columns having an upper area fraction between 24% and 78% are isotropic. Hexagonal arrays of circular columns having an upper area fraction between 6% and 75% are isotropic. Swapping the elevations, hexagonal arrays of circular depressions in a flat plate having an upper area fraction between 25% and 94% are isotropic. Hexagonal arrays of square columns having an upper area fraction between 4% and 49% are isotropic.

Plates with 15% elongated hexagonal arrays of cone or bump protrusions described in Schlichting [5] are also isotropic; L_P is near the geometric mean of the periods of the elongated axis and its perpendicular.

This isotropy test is not equivalent to the visual appearance of isotropy. Square post arrays having upper area fractions of 20% do not pass the isotropy test, while those with 30% do. Plates from Schlichting [5] having elongated hexagonal arrays of cones are not visually isotropic, but pass the isotropy test.

A plate surface is isotropic, periodic roughness when its $j_P \equiv L/L_P \gg 1$.

12. **Onset of rough turbulence**

For an isotropic, periodic roughness with $0 < \varepsilon < L_P \ll L$, there must be some value $Re_\lambda > 0$ such that when $0 < Re < Re_\lambda$, the fluid flow exhibits laminar or smooth turbulent behavior along the entire plate.

The boundary-layer is thinnest at the leading edge. Because the roughness is periodic, any disruption will start within the leading band ($0 < x < L_P$) of roughness. In this investigation, a boundary-layer is considered disrupted when $\varepsilon > \delta_2(L_P)$, where $\delta_2(x)$ is the boundary-layer momentum thickness at x.

$\delta_2(x)$ is the thickness of bulk flow having the same momentum flow rate as the plate's boundary-layer at x. Momentum thickness δ_2 is not a directly measurable quantity. Schlichting [9] gives the momentum thickness of laminar and smooth turbulent boundary-layers as formulas (36) and (37), respectively:

$$\delta_{2\lambda}(x) = 0.664\, x\, {Re_x}^{-1/2} = 0.664\, \sqrt{Re_x}\, \frac{L}{Re} \tag{36}$$

$$\delta_{2\sigma}(x) = 0.036\, x\, {Re_x}^{-1/5} = 0.036\, {Re_x}^{4/5}\, \frac{L}{Re} \tag{37}$$

Laminar $\delta_{2\lambda}$ formula (36) is from the Blasius boundary-layer model, which is well established. Smooth turbulent $\delta_{2\sigma}$ formula (37) is less certain.

Momentum thickness $\delta_2(x)$ is a local property of the fluid flow. In order to work locally with roughness Reynolds number Re_ε formula (29), change $L \to x$ and $Re \to Re_x$; then solve $Re_\varepsilon = 1$ for x/ε:

$$Re_\varepsilon = \frac{Re_x}{\sqrt{3}\,[x/\varepsilon]\,\ln(x/\varepsilon)} = 1 \qquad \frac{Re_x}{\sqrt{3}} = \frac{x}{\varepsilon}\,\ln\frac{x}{\varepsilon} \qquad \frac{x}{\varepsilon} = \exp\left(\mathrm{W}_0\left(\frac{Re_x}{\sqrt{3}}\right)\right) \tag{38}$$

Re_x grows proportionally to x; hence, the smooth turbulence momentum thickness $\delta_2(x)$ should be proportional to the product of x and formula (25) u_τ/u, the friction travel per run travel ratio:

$$\delta_2(x) \propto x\,\frac{u_\tau}{u} = \frac{x}{\sqrt{3}\,\ln(x/\varepsilon)} = \frac{x}{\sqrt{3}\,\mathrm{W}_0\left(Re_x/\sqrt{3}\right)} \tag{39}$$

The coefficient seems to be $1/3^3 \equiv 1/27 \approx 0.0370$:

$$\delta_2(x) = \frac{x}{3^3\,\mathrm{W}_0\left(Re_x/\sqrt{3}\right)} \qquad \sqrt{3}\,\mathrm{e} < Re_x \le Re \tag{40}$$

The occurrence of 3^3 may be related to the equivalence of φ^φ and $\exp(\varphi\,\ln\varphi)$.

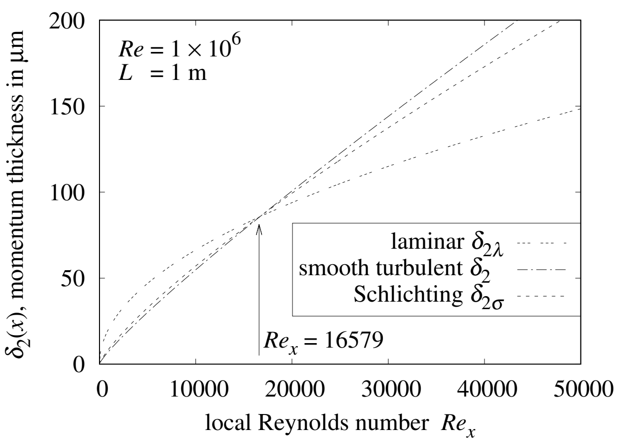

Figure 13 smooth plate $\delta_2(x)$ versus Re_x

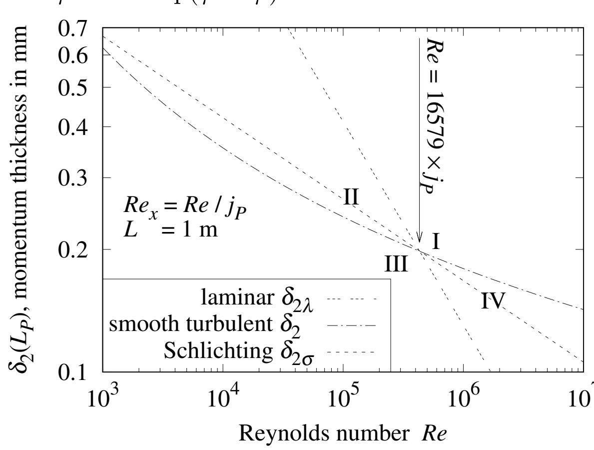

Figure 14 smooth plate $\delta_2(L_P)$ versus Re

Figure 13 demonstrates that "smooth turbulent δ_2" from equation (40) and $\delta_{2\sigma}$ from equation (37) are close to each other between the origin and the intersection of the laminar and turbulent curves at:

$$0.664\,\sqrt{Re_x} = 0.036\,{Re_x}^{4/5} \qquad Re_x = \left[\frac{0.664}{0.036}\right]^{10/3} \approx 16579 \tag{41}$$

Thus, $\delta_{2\sigma}(L_P)$ is a reasonable approximation for $\delta_2(L_P)$ in the leading band of roughness.

Figure 14 shows the (theoretical) momentum thickness of laminar and smooth turbulent flows along a 1 m long plate versus Re. The intersecting laminar $\delta_{2\lambda}$ and smooth turbulent δ_2 curves partition the graph into four regions marked I, II, III, and IV.

When the point at coordinates $[Re, \varepsilon]$ is in region I, the roughness is sufficient to disrupt both laminar and smooth turbulent flow; hence, leading band fluid flow will be rough turbulent.

When $[Re, \varepsilon]$ is in regions II or III, the roughness is not high enough to significantly disrupt laminar flow; hence, leading band fluid flow will be laminar, possibly transitioning to smooth turbulent.

When $[Re, \varepsilon]$ is in region IV, the roughness would be sufficient to disrupt laminar flow, but not large enough to disrupt smooth turbulent flow; hence, leading band fluid flow would be smooth turbulent.

With $\delta_{2\lambda} = \varepsilon$ and $x = L_P$, solve $\delta_{2\lambda}$ formula (36) for the laminar upper-bound Re_λ:

$$Re_\lambda = \left[\frac{0.664}{\varepsilon}\right]^2 L_P\, L \tag{42}$$

With $x = L_P$ and $\delta_2(x) = \varepsilon$ in δ_2 formula (40):

$$\varepsilon = \frac{L_P}{3^3\ \mathrm{W}_0\left(Re\, L_P/[\sqrt{3}\, L]\right)} \qquad \mathrm{W}_0\left(\frac{Re\, L_P}{\sqrt{3}\, L}\right) = \frac{L_P}{3^3\ \varepsilon} \qquad Re \gg \frac{\sqrt{3}\,\mathrm{e}\, L}{L_P} \tag{43}$$

The inverse of $\varphi = \mathrm{W}_0(\vartheta)$ is $\vartheta = \varphi \exp \varphi$. Solving for the smooth turbulent upper-bound $Re_\sigma = Re$:

$$\frac{Re\, L_P}{\sqrt{3}\, L} = \frac{L_P}{3^3\ \varepsilon} \exp \frac{L_P}{3^3\ \varepsilon} \qquad Re_\sigma = \frac{\sqrt{3}\, L}{3^3\ \varepsilon} \exp \frac{L_P}{3^3\ \varepsilon} \tag{44}$$

Equating Re_λ and Re_σ yields their intercept (found numerically):

$$0.664^2\, \frac{L_P}{\varepsilon} = \frac{\sqrt{3}}{3^3} \exp \frac{L_P}{3^3\ \varepsilon} \qquad \frac{L_P}{\varepsilon} \approx 194.3 \tag{45}$$

Region IV requires $L/\varepsilon > 20\, L_P/\varepsilon \approx 3886$. Machining precision must be much finer than this so that the roughness of each patch is larger than residual elevation errors. Region IV smooth turbulent flow will be rare; most isotropic, periodic roughness will transition directly from laminar to rough turbulent flow.

13. Plateau roughness

Disjoint flow mode regions can form along plates whose roughness peaks are all co-planar (at the same elevation) plateaus. With $Re > \max(Re_\sigma, Re_\lambda)$ producing rough turbulence in the leading band of the plate, smooth turbulent flow occurs downstream from where $\delta_2(x)$ is large enough to bridge the gaps. The drag from the downstream portion of the surface will be proportional to $\overline{f_\sigma}$, not the constant $\overline{f_\rho}$ of rough turbulent flow, making it a non-constant terminal drag coefficient as described by S. F. Hoerner in Hama [6].

Informally, a "plateau roughness" is an isotropic, periodic roughness with most of its area at its peak elevation. Of particular interest are plateau roughnesses where each cell contains a contiguous plateau area whose boundary has a convex perimeter within the cell. This will either be an array of "islands" whose tops are all co-planar, or an array of "wells" dropping below an otherwise flat plane.

Consider a smooth flat plate etched with a square grid of grooves subjected to a $Re > \max(Re_\sigma, Re_\lambda)$ flow. When the boundary-layer is disrupted by a groove perpendicular to the flow, the smooth turbulent boundary-layer restarts at the leading edge of the next island. At the scale of the roughness period L_P, the momentum thickness of the boundary-layer grows from 0 to nearly the L-scale $\delta_2(x)$ value (depending on the size of the island). If it grows to exceed ε, then the rest of the plate (to its trailing edge) will have a smooth turbulent skin-friction coefficient proportional to $\overline{f_\sigma}$.

Along isotropic roughness, the growth of δ_2 depends on plateau size, but not on orientation. In natural convection from an upward-facing horizontal plate [22, 23], the (isotropic) characteristic-length metric $L^* = A^*/p^*$ is the convex area A^* per its perimeter length p^* ratio. For a regular polygon or circle, $L^* = r/2$, where r is the minimum radius of the regular polygon or circle.

Multiplying both sides of δ_2 formula (40) by $3^3 Re/[\sqrt{3}\,L]$ allows Re_x to be isolated using the Lambert W_0 function identity $\varphi/\mathrm{W}_0(\varphi) = \exp\mathrm{W}_0(\varphi)$:

$$\frac{3^3 Re}{\sqrt{3}\,L}\,\delta_2 = \frac{Re_x/\sqrt{3}}{\mathrm{W}_0\left(Re_x/\sqrt{3}\right)} = \exp\mathrm{W}_0\left(\frac{Re_x}{\sqrt{3}}\right) \tag{46}$$

Let $\delta_2 = \varepsilon$ in order to find the island Re_x threshold Re_I. Turning to dimensional analysis, the Re strength needed to produce smooth turbulence grows with ε/L^* and with L/L_P. Substituting a product of powers of these ratios for Re into equation (46), then taking the logarithm of both sides:

$$Re = \frac{\varepsilon}{L^*}\left[\frac{L}{L_P}\right]^3 \qquad \ln\frac{3^3\,\varepsilon^2\,L^2}{\sqrt{3}\,L^*\,L_P^3} = \mathrm{W}_0\left(\frac{Re_x}{\sqrt{3}}\right) \tag{47}$$

The inverse of $\varphi = \mathrm{W}_0(\vartheta)$ is $\vartheta = \varphi\,\exp\varphi$. Solving formula (47) for $Re_I = Re_x$:

$$Re_I = Re_x = \frac{3^3\,\varepsilon^2\,L^2}{L^*\,L_P^3}\,\ln\frac{3^3\,\varepsilon^2\,L^2}{\sqrt{3}\,L^*\,L_P^3} \qquad \frac{[4\,L^*]^2}{L_P^2} > \frac{1}{2} \tag{48}$$

With large enough gaps, the islands are too short to support smooth turbulence bridging the gaps, leading to the inequality in formula (48). Formula (48) is tested against a square-grooved plate in Section 23.

Laying a perforated sheet on a flat plate turns the holes into wells. $L^* = A^*/p^*$ is the hole area A^* per its perimeter length p^* ratio. Flowing fluid must rise after diving into a well; hence, there are twice as many roughness interactions per cell. Instead of $Re = [\varepsilon/L^*]\,[L/L_P]^3$ in formula (47), let:

$$Re = \frac{\varepsilon}{L^*}\left[\frac{L}{2\,L_P}\right]^3 \qquad \ln\frac{3^3\,\varepsilon^2\,L^2}{2^3\,\sqrt{3}\,L^*\,L_P^3} = \mathrm{W}_0\left(\frac{Re_x}{\sqrt{3}}\right) \tag{49}$$

leading to the wells Re_x threshold Re_W:

$$Re_W = Re_x = \frac{3^3\,\varepsilon^2\,L^2}{2^3\,L^*\,L_P^3}\,\ln\frac{3^3\,\varepsilon^2\,L^2}{2^3\,\sqrt{3}\,L^*\,L_P^3} \qquad \frac{[4\,L^*]^2}{L_P^2} < \frac{1}{2} \tag{50}$$

With large enough wells, the flats between them are too narrow to support smooth turbulence bridging the wells, leading to the inequality in formula (50). Formula (50) is tested against perforated sheets in Section 22.

Let "openness" $0 < \Omega < 1$ be the non-plateau area per cell area ratio; $1 - \Omega$ is thus the "upper area fraction" in Section 11. Let $S_{s,t}$ be a $w \times w$ matrix of elevations. The span of elevations accepted as plateau must be a length smaller than ε and decrease with increasing L_P, which suggests ε^2/L_P:

$$\Omega \approx \frac{1}{w^2}\sum_{t=0}^{w-1}\sum_{s=0}^{w-1}\begin{cases}1, & \text{if } S_{s,t} < \max(S) - \varepsilon^2/L_P;\\ 0, & \text{otherwise.}\end{cases} \tag{51}$$

Circularity $o^* = 4\,\pi\,A^*/{p^*}^2 = 4\,\pi\,{L^*}^2/A^*$ takes its maximum value, 1, for disks; it is $\pi\,\sqrt{3}/6 \approx 0.907$ for hexagons, $\pi/4 \approx 0.785$ for squares, and $\pi\,\sqrt{3}/9 \approx 0.605$ for equilateral triangles. Being isotropic, L_P is non-directional; its effective cell area $A_P = \pi\,L_P^2/4$. Revisiting inequalities (48, 50):

$$\frac{1}{2} < \frac{[4\,L^*]^2}{L_P^2} = \frac{A^*}{A_P}\,\frac{4\,\pi\,A^*}{{p^*}^2} = [1-\Omega]\,o^* \qquad \Omega < 1 - \frac{1}{2\,o^*} \tag{52}$$

$$\frac{1}{2} > \frac{[4\,L^*]^2}{L_P^2} = \frac{A^*}{A_P}\,\frac{4\,\pi\,A^*}{{p^*}^2} = \Omega\,o^* \qquad \Omega < \frac{1}{2\,o^*} \tag{53}$$

Re_I equation (48) is valid when $\Omega < 1 - 1/[2\,o^*]$. Because $0 < o^* \le 1$, $1/2$ is the Ω upper-bound. When $\Omega > 1/2$, the flow will be rough turbulent. Re_W equation (50) is valid when $\Omega < 1/[2\,o^*]$. Ω can range above $1/2$ when $o^* < 1$; however, surfaces with $\Omega > 1/2$ and $o^* < 1$ do not pass the isotropy test (hexagonal array of square holes in Section 11). This suggests a quantitative definition of plateau roughness:

- "Plateau roughness" is an isotropic, periodic roughness with $\Omega < 1/2$.
- When $\Omega > 1/2$ and $Re > \max(Re_\sigma, Re_\lambda)$, flow along the entire surface will be rough turbulent. Thus it will have a constant terminal drag coefficient.
- Sand-roughness and the sphere roughness of Pimenta et al have $\Omega \approx 0.877 > 1/2$. Therefore, they are not plateau roughness, and will have constant terminal drag coefficients.

14. **Local skin-friction**

Conversions between local and average skin-friction are needed in order to compare prior with present work.

The ratio of average to local skin-friction $\overline{f_\sigma}/f_\sigma > 1$ of a continuous boundary-layer is calculated from f_σ by formula (54). The singularity (division by 0) at the leading edge of the plate is avoided by using $Re_0 > 0$ as the integration lower bound; Re_0 must be chosen such that $f_\sigma(Re_0) \ll 1$.

$$\frac{\overline{f_\sigma}(Re)}{f_\sigma(Re)} = \frac{1}{Re - Re_0} \int_{Re_0}^{Re} \frac{f_\sigma(Re_x)}{f_\sigma(Re)} \, \mathrm{d}Re_x \tag{54}$$

The local skin-friction coefficient is not well-defined for self-similar roughness because its L/ε is constant. Periodic roughness has varying L/ε; conveniently, it also provides L_P/ε as the lower-bound of integration.

A crucial difference between periodic roughness and smooth surfaces is that periodic roughness disrupts the boundary-layer repeatedly. Thus, the local skin-friction coefficients being averaged are independent. Instead of $\overline{f_\rho}/f_\rho$ accruing linearly, it should go as the square:

$$\frac{\overline{f_\rho}(L/\varepsilon)}{f_\rho(L/\varepsilon)} = \left[\frac{\varepsilon}{L - L_P} \int_{L_P/\varepsilon}^{L/\varepsilon} \frac{f_\rho(r)}{f_\rho(L/\varepsilon)} \, \mathrm{d}r \right]^2 \tag{55}$$

Applying formula (55) to the Mills-Hang local formula (9) yields the average skin-friction coefficient:

$$\overline{C_f}^2 \Big/ C_f \tag{56}$$

where C_f and $\overline{C_f}$ are from equations (9) and (10), respectively.

At $L/\varepsilon = 4000$ ($L/k_S = 750$), formula (56) has values in excess of 20% larger than the Mills-Hang $\overline{C_f}$ formula (10) derived using averaging formula (13). The average skin-friction coefficient was of minor importance in Mills and Hang [8]; the paper did not make comparisons with measurements of average skin-friction.

For disrupted boundary-layers, the transform for local friction f_ρ given average friction $\overline{f_\rho}$ is:

$$\frac{f_\rho(L/\varepsilon)}{\overline{f_\rho}(L/\varepsilon)} = \left[\frac{\mathrm{d}\big([L - L_P]\, \overline{f_\rho}(L/\varepsilon)\big)}{\mathrm{d}L} \Bigg/ \overline{f_\rho}(L/\varepsilon) \right]^2 \tag{57}$$

Applying formula (57) to $\overline{f_\rho}$ formula (28) for rough surfaces yields the local skin-friction coefficient:

$$f_\rho(x/\varepsilon) = \frac{1}{3} \left[\frac{\ln(x/\varepsilon) + 2\ [L_P/x - 1]}{\ln^2(x/\varepsilon)} \right]^2 \qquad L \ge x > L_P \ge \varepsilon \tag{58}$$

The local skin-friction coefficient for smooth turbulent flow f_σ can be derived from $\overline{f_\sigma}$ equation (32) and equations (59) provided that $Re_x \ge Re_0 \ge \sqrt{3}\,\mathrm{e}$ and $Re_x \gg \sqrt{3}\,\mathrm{e}$:

$$\frac{\mathrm{dW_0}(\vartheta)}{\mathrm{d}\vartheta} = \frac{\mathrm{W_0}(\vartheta)}{\vartheta\ [\mathrm{W_0}(\vartheta) + 1]} \qquad f_\sigma(Re_x) = \frac{\mathrm{d}\big([Re_x - Re_0]\, \overline{f_\sigma}(Re_x)\big)}{\mathrm{d}Re_x} \tag{59}$$

$$f_\sigma(Re_x) = \frac{\sqrt[3]{2}}{3} \frac{\mathrm{W_0^2}\left(Re_x/\sqrt{3}\right) - 2\,[1 - Re_0/Re_x]\ \mathrm{W_0}\left(Re_x/\sqrt{3}\right) - 1}{\left[\mathrm{W_0}\left(Re_x/\sqrt{3}\right) - 1\right]^3\ \left[\mathrm{W_0}\left(Re_x/\sqrt{3}\right) + 1\right]} \tag{60}$$

Figure 15 plots local smooth turbulent skin-friction coefficient formulas and measurements collected in Churchill [11]. The measurements have 1.9% RMSRE versus “present work” formula (60).

When calculating RMSRE, the error due to variation at a single point is larger than the error when that variation is split among multiple points. Thus, local measurements tend to have larger RMSRE than average measurements do. In Figure 15, the primary error contributor is the value at $Re_x = 10^7$.

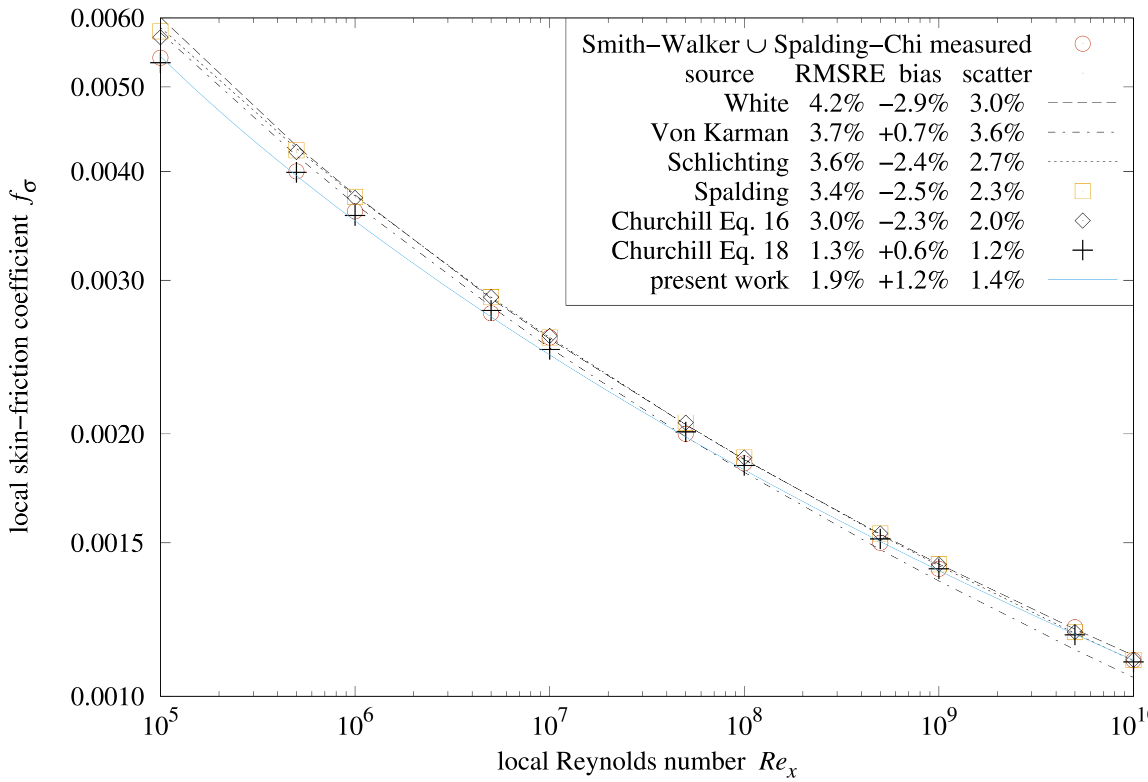

Figure 15 local f_σ versus Re_x of smooth plate

15. Forced convection from an isothermal rough plate

Forced convective heat transfer is expressed as the dimensionless average ($\overline{Nu}$) or local (Nu) Nusselt number. Heat transfer by rough turbulence will grow with the amount of turbulence induced, $\overline{f_\rho}\, Re$. It will also grow with $Pr^{1/3}$. The fluid's Prandtl number (Pr) is the kinetic viscosity per thermal diffusivity ratio. Fluids with large Pr transport heat in the fluid flow; conduction is dominant in fluids with small Pr. The 1/3 exponent for Pr may relate to it being a property of the fluid in three dimensions. Heat transfer from the trailing part of the plate is reduced due to fluid heating by the leading part; hence, convection will be scaled by 1/2. Expanding $\overline{f_\rho}$ from equation (28) yields formula (61) for rough turbulent average forced convection:

$$\overline{Nu_\rho} = \frac{\overline{f_\rho}\, Re\, Pr^{1/3}}{2} = \frac{Re\, Pr^{1/3}}{6\, \ln^2 (L/\varepsilon)} \qquad \frac{L}{\varepsilon} \gg 1 \qquad Pr > 0 \tag{61}$$

The present analysis for self-similar $\overline{f_\rho}$ did not involve boundary-layers; hence, it avoids the $Pr > 0.6$ restriction affecting formula (62). Formula (61) is compared with measurements in Section 23.

16. Forced convection from an isothermal smooth plate

For smooth turbulent convection, Lienhard [24] recommends composing the Gnielinski formula (62) with the White smooth formula (12) for C_σ.

$$Nu = \frac{Re_x\, Pr\, C_\sigma/2}{1 + 12.7\, [Pr^{2/3} - 1]\, \sqrt{C_\sigma/2}} \approx \frac{Re_x\, Pr\, C_\sigma/2}{1 + 9\, [Pr^{2/3} - 1]\, \sqrt{C_\sigma}} \qquad Pr \geq 0.6 \tag{62}$$

Lienhard states that Nu formula (63) has similar accuracy for gases:

$$Nu = 0.0296\, {Re_x}^{4/5}\, Pr^{0.6} \qquad 0.6 \leq Pr < 2 \tag{63}$$

$$\overline{Nu} = 0.037\, Re^{4/5}\, Pr^{0.6} \qquad 0.6 \leq Pr < 2 \tag{64}$$

Forced convection is similar to natural convection from a vertical plate; in both, fluid flows parallel to the plate's characteristic-length axis, and is uniform across the plate's other axis.

Jaffer [25] finds that stationary fluid conducts heat from the plate with an effective Nusselt number Nu_0, which is a coefficient factor of both the static and flow-induced heat transfer terms:

$$Nu_0 = \frac{2^4}{\pi^2 \sqrt[4]{2}} \approx 1.363 \tag{65}$$

Flow-induced heat transfer grows with $Nu_0\, Re\, \overline{f_\sigma}$. Because this heat traverses boundary-layers, the Pr dependence is more complicated than $Pr^{1/3}$. In Jaffer [25], the vertical-plate natural convection dependence is $\sqrt[3]{Pr/\Xi(Pr)}$, where $\Xi(Pr)$ is defined using ℓ^p-norm definition (66) with $p = \sqrt{1/3}$:

$$\|\varphi, \vartheta\|_p \equiv \left(|\varphi|^p + |\vartheta|^p\right)^{1/p} \tag{66}$$

$$\Xi(Pr) = \left\|1,\ \frac{0.5}{Pr}\right\|_{\sqrt{1/3}} \tag{67}$$

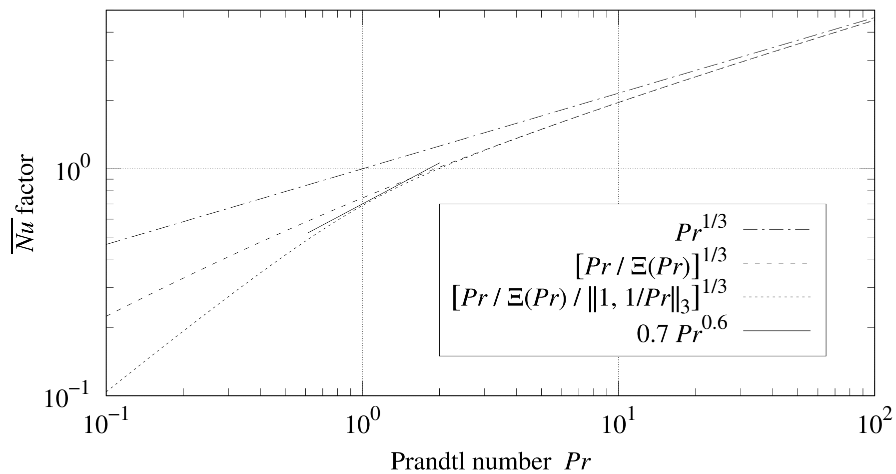

Figure 16 smooth plate $\overline{Nu_\sigma}$ dependence on Pr

In Figure 16, $\sqrt[3]{Pr/\Xi(Pr)}$ is asymptotically $Pr^{1/3}$ for large Pr and $\sqrt[3]{2}\, Pr^{2/3}$ for small Pr. At small Pr, conduction does not amplify forced convection as it does for natural convection; the Pr exponent should be 1. An additional factor using the ℓ^3-norm accomplishes this. Formula (68) is asymptotically $\sqrt[3]{2}\, Pr$ for $Pr \ll 0.5$. The "$0.7\, Pr^{0.6}$" trace shows that formula (68) has a slope close to formulas (63, 64) for gases.

$$\sqrt[3]{\frac{Pr}{\Xi(Pr)}}\ \sqrt[3]{\frac{1}{\|1, 1/Pr\|_3}} \tag{68}$$

The slope of formula (62) $Nu(C_\sigma)$ decreases with increasing Pr; for large Pr, $Nu \propto \sqrt{C_\sigma}$. Recall from equations (26, 27) that $\overline{f_c} \propto u_\tau^2$; hence $\sqrt{\overline{f_c}} \propto u_\tau$. This indicates that transport through the boundary-layer limits convection at large Pr. In order to reduce the asymptotic dependence from $\overline{f_\sigma}$ to $\sqrt{\overline{f_\sigma}}$, the convection formula will include a factor which takes the square-root of an expression gating $\overline{f_\sigma}$ by Pr:

$$\sqrt{\overline{f_\sigma}}\ \sqrt{\frac{Pr/\sqrt{162} + 1}{\sqrt{162}\, Pr + 1/\overline{f_\sigma}}} \qquad \sqrt{162} = 9\sqrt{2} \approx 12.7 \tag{69}$$

The scaling for upstream heating was 1/2 in $\overline{Nu_\rho}$ formula (61) for disruptive roughness; the smooth turbulent boundary-layer reduces this interaction; $\sqrt{1/3} \approx 0.577$ appears correct in the smooth case.

Formula (70) is proposed for smooth turbulent convection for all $Pr > 0$:

$$\overline{Nu_\sigma} = \frac{Nu_0\, Re}{\sqrt{3}} \sqrt{\frac{\overline{f_\sigma}\ \left[Pr/\sqrt{162} + 1\right]}{\sqrt{162}\, Pr + 1/\overline{f_\sigma}}}\ \sqrt[3]{\frac{Pr/\Xi(Pr)}{\|1, 1/Pr\|_3}} \qquad Re \gg \sqrt{3}\,\mathrm{e} \tag{70}$$

Lienhard [24] compares the Gnielinski-White convection formula with local measurements from studies of fluids with $0.7 \le Pr \le 257$ spanning $4000 < Re_x < 4.3 \times 10^6$. The smallest turbulent Re_x was $\approx 10^5$. Formula (63) is more accurate than Gnielinski-White for turbulent air ($Pr \approx 0.71$) at $Re_x < 10^5$.

Figures 17 and 18 show $\overline{Nu_\sigma}$ versus Pr and Re, respectively. The "present work" traces are formula (70). The "averaged" traces use formula (71) to numerically average the composition of the Gnielinski formula (62) with the White formula (12).

$$\overline{Nu_\sigma}(Re) = \int_{Re_0}^{Re} \frac{Nu_\sigma(Re_x)}{Re_x}\,\mathrm{d}Re_x \tag{71}$$

$\overline{Nu_\sigma}$ formula (70) matches the numerically averaged Gnielinski-White formula within $\pm 6.6\%$ over the range $10^5 < Re < 4.3 \times 10^6$ with $4.0 \le Pr \le 257$. At $Pr = 0.71$, $\overline{Nu_\sigma}$ matches gases formula (64) within $\pm 4\%$ over the range $10^4 < Re < 4.3 \times 10^6$. Over the same ranges, local convection Nu_σ formula (72) matches formulas (62) and (63) within $\pm 7.1\%$. Figure 19 shows Nu_σ and Gnielinski formula (62) versus Re_x.

$$Nu_\sigma(Re_x) = Re_x \frac{\mathrm{d}\overline{Nu_\sigma}(Re_x)}{\mathrm{d}Re_x} \tag{72}$$

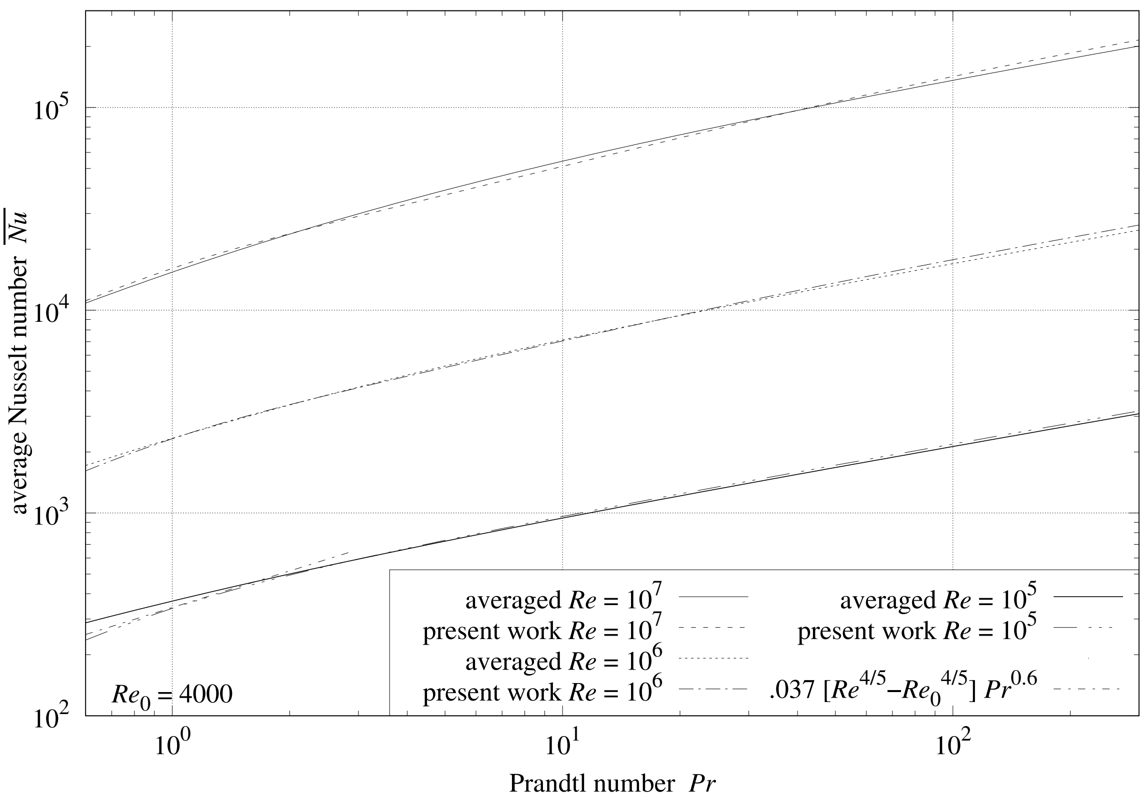

Figure 17 smooth plate average turbulent convection versus Pr

Adapting the Lienhard [24] comprehensive smooth plate convection formula to use Nu_σ formula (72):

$$\begin{gathered} Nu(Re_x) = \left\| Nu_\lambda(Re_x), \left\| \left[\frac{Re_x}{Re_l}\right]^c Nu_\lambda(Re_l), Nu_\sigma(Re_x) \right\|_{-10} \right\|_5 \\ Nu_\lambda(Re_x) = 0.332\sqrt{Re_x}\,Pr^{1/3} \qquad c = 0.9922\,\log_{10} Re_l - 3.013 \end{gathered} \tag{73}$$

where $Re_l < 2.8 \times 10^6$ is the plate-specific upper-bound for purely laminar flow. For a periodic roughness with $Re_\sigma < Re_\lambda$, it seems likely that $Re_l = Re_\sigma$.

Having Nu_σ in place of Gnielinski-White, formula (73) should work for both gasses and liquids.

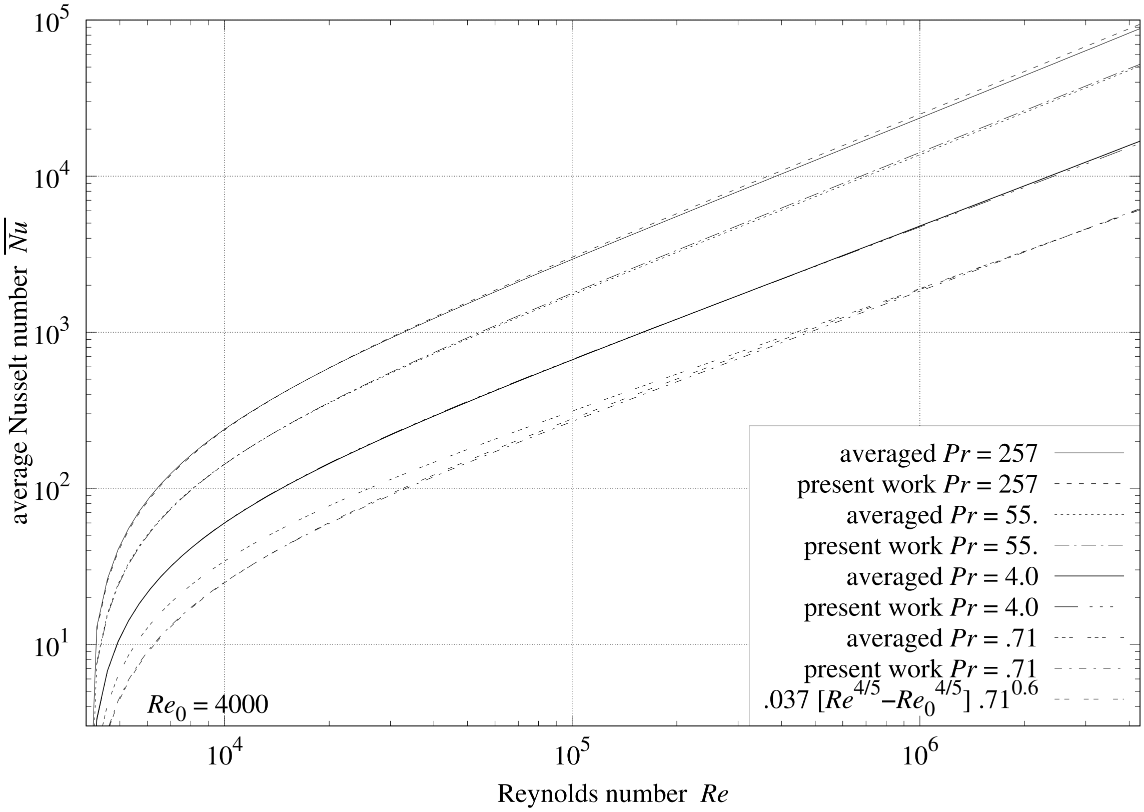

Figure 18 smooth plate average turbulent convection versus Re

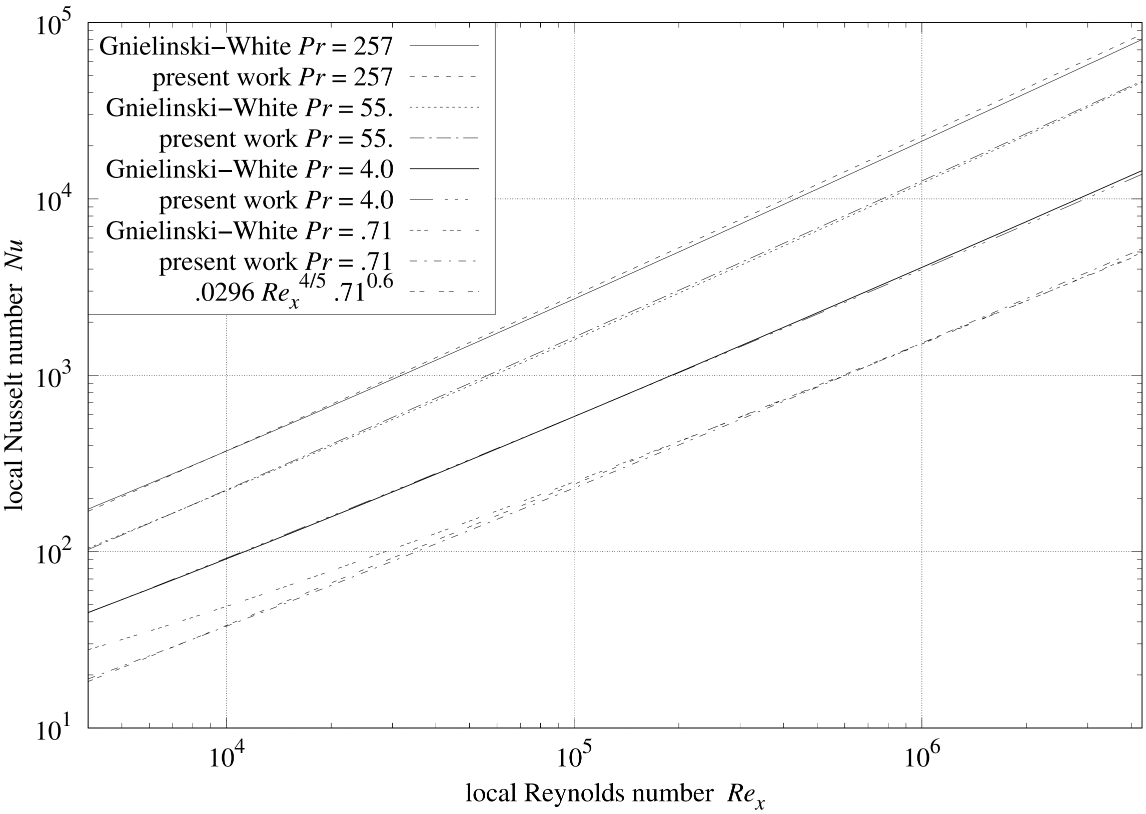

Figure 19 smooth plate local turbulent convection versus Re_x

17. Periodic smoothness and rough laminar flow

Flow along a flat, single-crystal silicon wafer should exhibit smooth formula (73) behavior. At atomic scale, however, it is an isotropic, periodic roughness with $L_p = 543$ nm and $\varepsilon = 31.2$ nm. Is it rough or smooth?

The amount of laminar flow displaced by a periodic roughness grows with both ε and L_P. Dimensional analysis suggests that this displacement is significant when $L/\sqrt{\varepsilon\, L_P} < Re_\sigma$. Plates with $L/\sqrt{\varepsilon\, L_P} > Re_\sigma$ can be considered "smooth", behaving as formula (73) when $Re < Re_\lambda$. Table 2 compares parameters of several surface geometries. The "silicon wafer" row has $L/\sqrt{\varepsilon\, L_P} > Re_\sigma$, indicating that it is smooth.

	L/L_P	L/ε	$L/\sqrt{\varepsilon\, L_P}$		Re_σ		Re_λ
silicon wafer	5.62×10^5	9.78×10^6	2.34×10^6	$>$	1.19×10^6	$\ll$	7.50×10^7
cloth tape (dull)	1.32×10^2	8.82×10^3	1.08×10^3	$<$	6.70×10^3	$\ll$	2.59×10^5
cloth tape (shiny)	1.54×10^2	7.08×10^3	1.04×10^3	$<$	2.49×10^3	$\ll$	1.43×10^5
Pimenta et al	1.72×10^3	1.47×10^4	5.02×10^3	$>$	1.29×10^3	$\ll$	5.51×10^4
bi-level $\varepsilon = 1$ mm	2.60×10^1	2.96×10^2	8.77×10^1	$>$	2.89×10^1	$\ll$	1.48×10^3
bi-level $\varepsilon = 3$ mm	2.60×10^1	1.02×10^2	5.14×10^1	$>$	7.55×10^0	$\ll$	1.76×10^2

Table 2 dimensionless parameters

Now consider $L/\sqrt{\varepsilon\, L_P} < Re_\sigma$. Tuck and Kouzoubov [26] finds that a slow laminar flow over a periodic roughness "...represents a shift of the apparent plane boundary toward the flow domain." At small Re, the rough laminar flow from the apparent boundary plane outward is the same as smooth laminar flow.

Between the surface and its apparent boundary plane, however, shearing stress periodically (L_P) exceeds that of a smooth surface, becoming more likely to spawn vortexes as Re increases, asymptotically approaching smooth turbulent flow. Heat transfer "processes which vary uniformly between ... limiting cases" (Churchill and Usagi [27]) suggests treating "rough laminar" convection as a competition between laminar convection $\overline{Nu_\lambda}$ and smooth turbulent convection $\overline{Nu_\sigma}$.

If the laminar and turbulent flows were perpendicular, their convection processes would combine as root-sum-squared, the ℓ^2-norm; but these flows are aligned. Independent processes combine as the ℓ^1-norm (addition); but these processes are competitive. An intermediate strength is needed. The geometric mean of 1 and 2 is $\sqrt{2}$; hence, the $\ell^{\sqrt{2}}$-norm is proposed for this mild competition:

$$\overline{Nu} = \left\|\overline{Nu_\lambda}, \overline{Nu_\sigma}\right\|_{\sqrt{2}} \qquad \overline{Nu_\lambda} = 0.664\,\sqrt{Re}\,Pr^{1/3} \tag{74}$$

$$Nu = \left\|Nu_\lambda, Nu_\sigma\right\|_{\sqrt{2}} \qquad Nu_\lambda = 0.332\,\sqrt{Re_x}\,Pr^{1/3} \tag{75}$$

$\overline{Nu_\lambda}$ and Nu_λ derive from the Blasius laminar model in Schlichting [9].

Section 24 tests formula (74). A skin-friction formula was not conjectured for lack of experimental data.

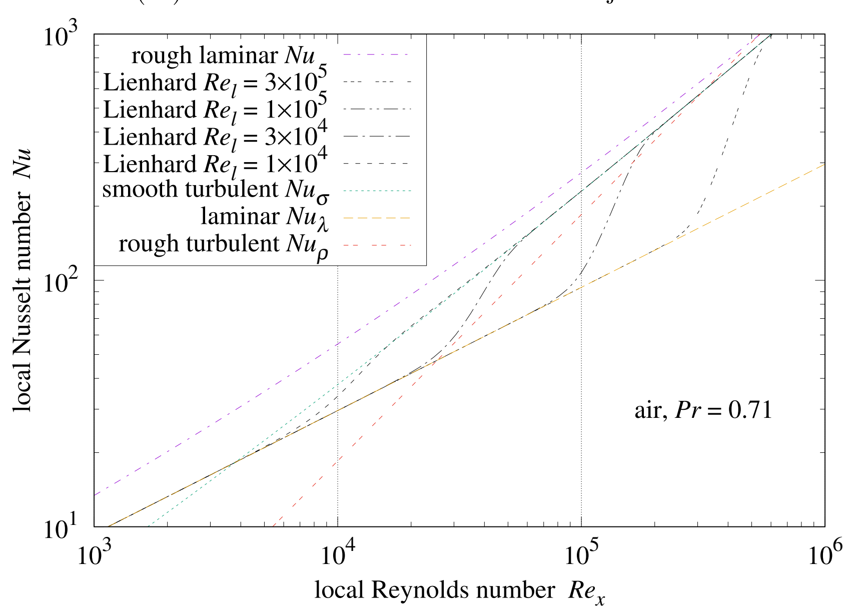

Figure 20 laminar to smooth turbulent convection transitions

Figure 20 shows the local rough laminar convection predicted by applying $\overline{Nu_\sigma} \to Nu_\sigma$ transform (72) to the rough laminar convection formula (74). It is indistinguishable from formula (75) at the scale of Figure 20. Also shown is "Lienhard" formula (73) at four Re_l values, smooth turbulent and laminar convection, and cloth tape geometric mean $L/\varepsilon \approx 7902$ rough convection (as if $Re > Re_\lambda$).

18. Turbulent flow modes

Isotropic, periodic surfaces with $Re_\sigma < Re_\lambda$ and $\Omega > 1/2$ shed the rough turbulence of formulas (28, 58, 61) when $Re > Re_\lambda$.

Isotropic, periodic roughness with $\Omega < 1/2$ is plateau roughness, shedding either smooth or rough turbulence, or a combination, when $Re > Re_\lambda$. Table 3 proposes the behaviors of plateau islands and plateau wells when $Re > Re_\lambda$:

condition	plateau islands	plateau wells
$[4\,L^*]^2/L_P^2 < 1/2$	rough formulas (28, 58, 61)	
$Re_x < Re_I$	rough formulas (28, 58, 61)	
$Re_x > Re_I$	smooth formula (76)	
$[4\,L^*]^2/L_P^2 > 1/2$		rough formulas (28, 58, 61)
$Re_x < Re_W$		blend formulas (77, 78)
$Re_x > Re_W$		smooth formula (79)

Table 3 turbulent flow modes for plateau roughness

The uppermost flow mode satisfying the inequality to its left takes precedence. The Re_x conditions split the plate at distance x from the leading edge into two regions operating in different modes.

The islands threshold Re_I is formula (48); the wells threshold Re_W is formula (50).

The "$Re_x > Re_I$" condition for islands is smooth turbulence with characteristic-length L_P. The island's area is augmented by 1/2 of the non-plateau area combined with $2\,\varepsilon\,[4\,L^*]$ using the ℓ^2-norm:

$$\overline{Nu} = \left\{1 - \Omega + \left\| \frac{\Omega}{2}, \frac{2\,\varepsilon\,[4\,L^*]}{L_P^2} \right\|_2 \right\} \frac{L}{L_P}\,\overline{Nu_\sigma}\left(\frac{Re\,L_P}{L}\right) \tag{76}$$

Convection measurements from a square grooved bi-level plate are compared with formula (76) in Section 23.

In plateau wells "blend" mode, the perforated sheet's plateau area is shedding smooth turbulence while its wells are in rough turbulence. The effective friction coefficient is the area-proportional blend:

$$\overline{f_c} = \Omega\,\overline{f_\rho}(L/\varepsilon) + [1-\Omega]\,\overline{f_\sigma} \tag{77}$$

$$f_c = \Omega\,\overline{f_\rho}(L/\varepsilon) + [1-\Omega]\,f_\sigma \tag{78}$$

Where $Re_x > Re_W$ along a perforated sheet, the friction is smooth turbulent, but with additional area $2\,\pi\,\varepsilon\,[4\,L^*]$ from the rims. Although the rim and sheet are perpendicular, the same flow brushes by both. A strength between ℓ^2 and $\ell^{\sqrt{2}}$ is needed; their geometric mean is $p = \sqrt[4]{8} \approx 1.682$:

$$f_c = \left\| 1, \frac{2\,\pi\,\varepsilon\,[4\,L^*]}{L_P^2} \right\|_{\sqrt[4]{8}} f_\sigma \tag{79}$$

Local resistance measurements of perforated sheets are compared with formulas (78, 79) in Section 22.

An analogous skin-friction formula for plateau islands could be conjectured, but is omitted because of the lack of measurement data for that configuration.

Convection formulas for plateau wells are also omitted for lack of measurement data.

Table 3 is specific to isotropic, periodic roughness. The rough turbulent mode uses formulas (28, 58, 61), which were developed for self-similar roughness, even though self-similar roughness is not periodic.

If measurements over a range of Re values from diverse plates with isotropic, periodic roughness are close to predictions by formulas for self-similar roughness, then it would be evidence that these formulas reflect a physical law of turbulent flow along isotropic surface roughness.

No self-similar roughness was tested in the present or prior works.

19. **Fully rough regime**

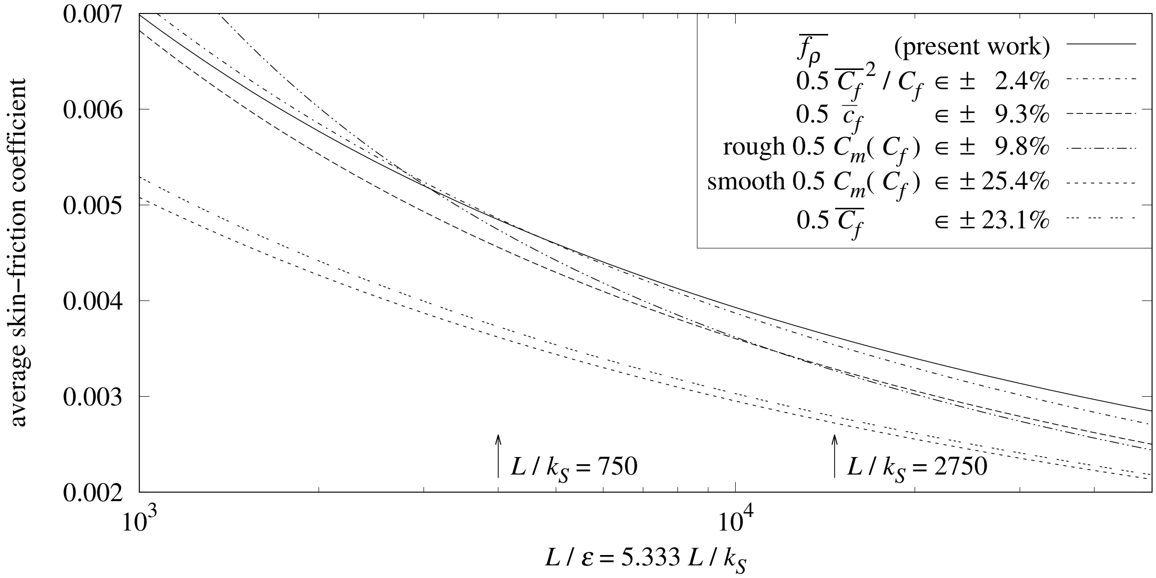

Figure 21 average friction coefficient of sand-roughness

Figure 21 compares fully rough regime average skin-friction formulas. To the right of each "$\in \pm$" is the maximum discrepancy from "$\overline{f_\rho}$ (present work)" equation (28) over the Mills-Hang range $750 < L/k_S < 2750$, which is $4000 < L/\varepsilon < 14666$.

Starting from the bottom of the Figure 21 key, "0.5 $\overline{C_f}$" is 1/2 of the Mills-Hang average formula (10).

The two "0.5 $C_m(C_f)$" traces are 1/2 of the Churchill smooth and rough averaging formulas (14) and (15) applied to the Mills-Hang local formula (9).

"0.5 $\overline{c_f}$" is 1/2 of the Prandtl-Schlichting average formula (8).

"0.5 $\overline{C_f}^2/C_f$" is 1/2 of formula (56), the disrupted boundary-layer averaging formula (55) applied to the Mills-Hang local formula (9); it is within ±2.4% of "$\overline{f_\rho}$ (present work)".

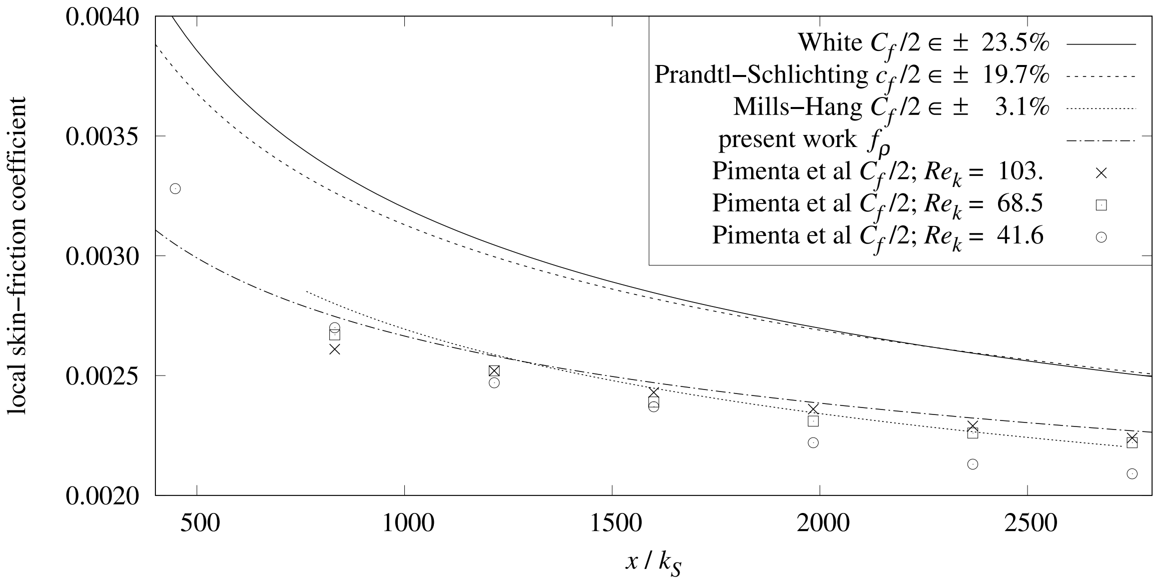

Figure 22 local friction coefficient of sphere-roughened plate

Figure 22 plots the fully rough local skin-friction coefficients from White (11), Prandtl-Schlichting (7), Mills-Hang (9), and the present work f_ρ formula (58). The maximum magnitude discrepancy between Mills-Hang and the present theory is 3.1% over the Mills-Hang range $750 < x/k_S < 2750$.

The points labeled "Pimenta et al" in Figure 22 show the local drag coefficient measurements versus x/k_S for the sphere-roughened plate at three rates of flow, $Re_k = 41.6$, 68.5, and 103. Table 4 gives the RMS error of this set of 19 measurements relative to each of the rough regime formulas:

source	formula	RMSRE	bias	scatter	count
Prandtl and Schlichting [3]	(7) $c_f/2$	15.6%	-15.4%	2.6%	19
Mills and Hang [8]	(9) $C_f/2$	3.7%	-2.4%	2.8%	19
White [10]	(11) $C_f/2$	16.6%	-16.3%	3.3%	19
present work	(58) f_ρ	4.5%	-3.0%	3.3%	19

Table 4 local friction coefficient of sphere-roughened plate

Having $L_P/\varepsilon < 194$, Re_λ formula (42) predicts that fluid flow along the entire sphere-roughened plate transitions directly from laminar to rough turbulence at $Re_\lambda \approx 24640$; but the smallest reported Re_x for the plate was 3.8×10^5.

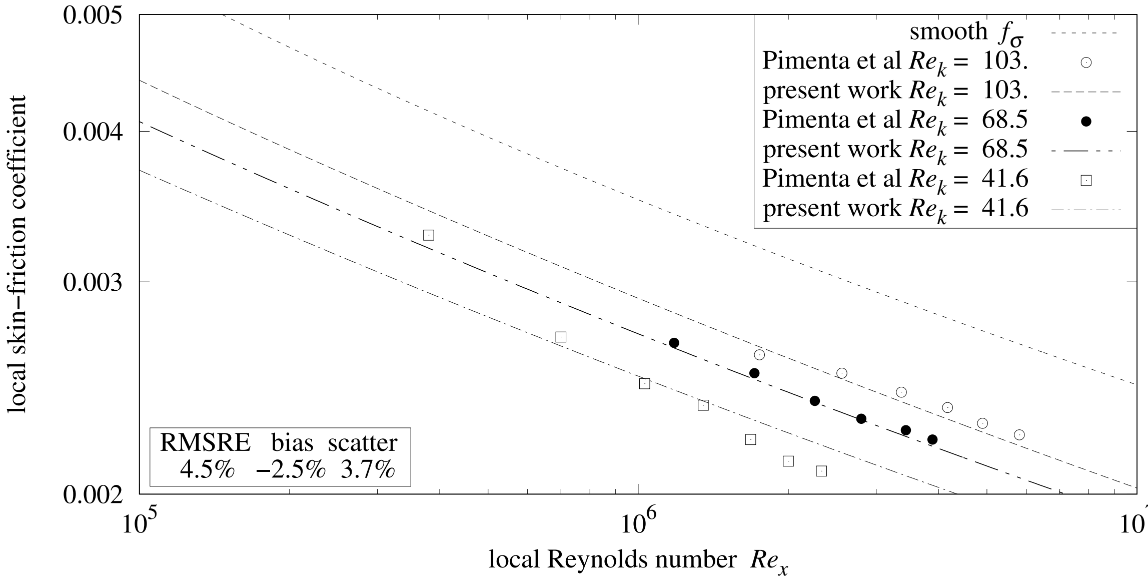

Figure 23 local f_ρ versus Re_x of sphere-roughened plate

Formula (38) calculates x/ε from the Re_x and $Re_\varepsilon = Re_k/5.333$ values supplied by Pimenta et al [7]. Figure 23 plots local $f_\rho(x/\varepsilon)$ versus Re_x (grouped by Re_k) for the sphere-roughened plate. Compared with the present theory, these measurements have an RMSRE of 4.5%, -2.5% bias, and 3.7% scatter. The bias and scatter differ from Table 4 because it is parameterized by x/k_S, while Figure 23 is parameterized by Re_x.

Despite the present work f_ρ formulas being derived from an analysis of self-similar roughness, they show fidelity to $C_f/2$ measurements of the periodic sphere-roughened plate versus x/k_S and Re_x. This supports the assertion that these formulas are intrinsic to turbulent flow along isotropic, periodic roughness.

20. **Smooth plate and sandpaper**

Bergstrom et al [14] has skin-friction coefficient measurements of sandpapers, woven wire meshes, and perforated sheets attached to a smooth plate, and also the 1.67 m × 1.16 m smooth plate alone. Skin-friction measurements were derived from Pitot probe measurements of air velocity at locations which were 1.3 m downwind from the leading edge of the plate. Bergstrom et al [14] estimated 5% as the combined measurement uncertainty of the smooth surface friction coefficient, and 9% for the rough surfaces.

The measurement tables in [14] include a column for free-stream velocity, U_e. In order to compute the Reynolds number $Re = U_e\,L/\nu$ from U_e, the kinematic viscosity $\nu = 16 \times 10^{-6}$ m^2/s was calculated for air at 20°C and the mean atmospheric pressure at the University of Saskatchewan, 95 kPa.

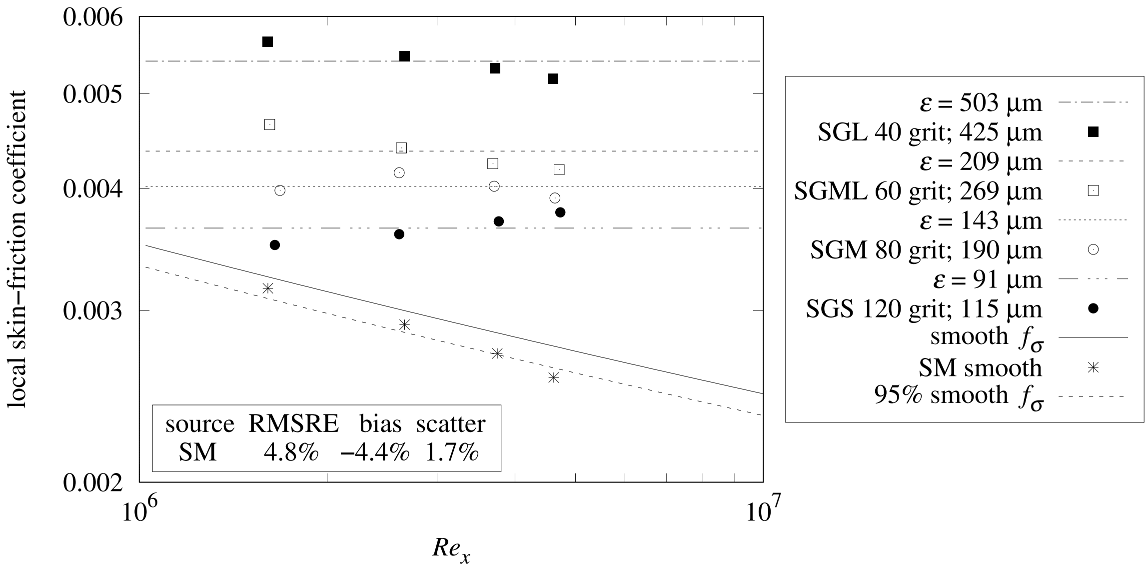

Figure 24 local f_ρ versus Re_x of sandpaper

Three of the four smooth plate measurements are within the 5% band, as shown by the points labeled "SM smooth" in Figure 24. The RMSRE versus f_σ formula (60) is 4.8%.

Microscopic examination of coarse grades of sandpaper reveals glued mounds of grits and canyons having depths which are several times the mean grit diameter. Sandpaper grit mean diameter is standardized, but not the height-of-roughness of the mounds; it could vary by manufacturer and lot. The horizontal traces in Figure 24 show that skin-friction coefficients which are independent of Re_x, as in the present theory, can be within the 9% estimated measurement uncertainty of the data.

The RMS height-of-roughness ε of sandpaper is much larger than ε of sand-roughness with the same mean grit diameter. For example, 40 grit sandpaper has a friction coefficient consistent with $\varepsilon \approx 503\,\mu$m, while $k_S = 425\,\mu$m sand-roughness would have $\varepsilon = k_S/5.333 \approx 80\,\mu$m.

21. **Woven wire mesh**

wire diameter d	center spacing s	$[s-d]^2/s^2$	$[s-\sqrt{2}\,d]^2/s^2$	openness in [14]	
1.04 mm	3.68 mm	52%	36%	35%	WML
0.58 mm	1.77 mm	45%	29%	30%	WMM
0.36 mm	1.68 mm	62%	49%	44%	WMS
0.36 mm	1.48 mm	58%	44%		
0.56 mm	1.68 mm	44%	28%		

Table 5 wire mesh dimensions

Woven wire meshes are specified by wire diameter d and wire center spacing s. Bergstrom et al [14] calculate mesh openness as $[s-\sqrt{2}\,d]^2/s^2$ instead of the $[s-d]^2/s^2$ formula used by manufacturers. Table 5 lists the dimensions and openness from [14] along with openness calculated both ways. The WML and WMM meshes have $[s-\sqrt{2}\,d]^2/s^2$ values close to [14]. The WMS mesh has $[s-\sqrt{2}\,d]^2/s^2 \approx 49\%$, versus 44% from [14]. If the 1.68 mm spacing were instead 1.48 mm, WMS would have $[s-\sqrt{2}\,d]^2/s^2 \approx 44\%$, but significantly less friction coefficient than the WMS measurements in Figure 25. A 0.36 mm wire diameter has conventional openness $[s-d]^2/s^2 \approx 44\%$ and matches the WMS data and the WMM trace and data.

There are periodic gaps between the wires and the plate; so the mesh-plate combination is not strictly a roughness. With the gaps filled, the RMS height-of-roughness ε would be:

$$
\begin{aligned}
z(x,y) &= \sqrt{\frac{d^2}{4}-x^2}+d-\frac{d}{2}\cos\frac{\pi\,y}{s} \qquad \overline{z}=\frac{4}{s^2}\int_{d/2}^{s}\int_{0}^{d/2} z(x,y)\,\mathrm{d}x\,\mathrm{d}y \\
\varepsilon &= \frac{4}{s^2}\int_{d/2}^{s}\int_{0}^{d/2} \left|z(x,y)-\overline{z}\right|^2\,\mathrm{d}x\,\mathrm{d}y+\frac{(s-d)^2\,\overline{z}^2}{s^2}
\end{aligned}
\tag{80}
$$

The periodic gaps between wires and the plate increase the flow's shearing stress. Scaling ε by the square root of the filled-gap side area per side area ratio is an increase of about 26% for these meshes:

$$\varepsilon' = \varepsilon\sqrt{\frac{12\,s+\pi\,d}{8\,s}} \tag{81}$$

The "unscaled 1.04 mm, 3.68 mm" trace in Figure 25 shows the predicted WML friction without this scaling.

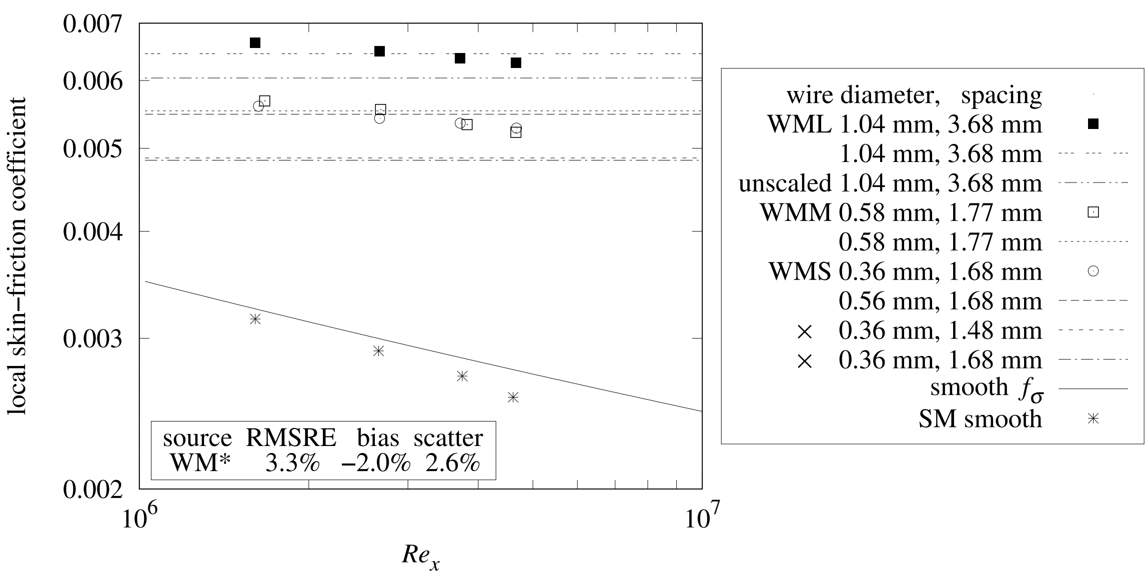

Figure 25 local f_ρ versus Re_x of woven wire mesh

Using (scaled) ε', the WML and WMM measurements match the present theory well within the ±9% estimated measurement uncertainty. The WMS measurements do not match unless a hypothesized single digit misprint in [14] is corrected, changing the wire diameter from 0.036 mm to 0.056 mm.

Taken together, the three (corrected) wire meshes have 3.3% RMSRE versus the present theory.

22. Perforated sheet

hole diameter d	center spacing s	square openness	hexagonal openness	openness in [14]	
$2.0\,\text{mm} \approx 5/64$	$2.81\,\text{mm} \approx 7/64$	39.8%	45.9%	45%	PL
$1.6\,\text{mm} \approx 4/64$	$2.43\,\text{mm} \approx 6/64$	34.1%	39.3%	41%	PM
$1.2\,\text{mm} \approx 3/64$	$3.40\,\text{mm} \approx 8.6/64$	9.8%	11.3%	<u>22%</u>	PS
$1.7\,\text{mm} \approx 4.3/64$	$3.40\,\text{mm} \approx 8.6/64$	19.6%	<u>22.7%</u>		
$1.2\,\text{mm} \approx 3/64$	$2.40\,\text{mm} \approx 6/64$	19.6%	<u>22.7%</u>		

Table 6 perforated sheet openness

Table 6 checks the openness of the perforated sheets from Bergstrom et al [14]. It finds that the holes were hexagonally arrayed. However, the PS sheet's calculated openness is 1/2 of the paper's 22%. There are two single digit changes, either of which results in hexagonal openness near 22%: hole diameter $d = 1.7\,\text{mm}$ or center spacing $s = 2.4\,\text{mm}$.

North American suppliers of perforated sheet metal generally specify hole diameter and center spacing in terms of 1/64 of an inch. Table 6 provides dimensions both ways. $d = 3/64$ with $s = 6/64$ is a standard size; $d = 4.3/64$ with $s = 8.6/64$ is not. Replacing PS row $s = 3.40$ mm with $s = 2.40$ mm:

$[4\,L^*] = d$	$L_P = s$	thickness	openness Ω		d^2/s^2	ε	Re_W
2.0 mm	2.81 mm	0.90 mm	45.9%	PL	0.507	0.449 mm	2.06×10^6
1.6 mm	2.43 mm	0.90 mm	39.3%	PM	0.434	0.441 mm	4.17×10^6
1.2 mm	2.40 mm	0.76 mm	22.7%	PS	0.250	0.318 mm	2.80×10^6

Table 7 perforated sheet parameters

Table 7 shows the dimensions and metrics of the perforated sheets when laid on the flat plate. For PL, $[4\,L^*]^2/L_P^2 = d^2/s^2 \approx 0.507 > 1/2$; its flow will be rough turbulent. The "$f_\rho(2898) = 0.0052$" trace in Figure 26 shows the predicted local skin-friction coefficient's close proximity to the PL measurements. The "$\times$ 2.00 mm, 2.81 mm, 0.90 mm" trace with transition at "PL$\times$" shows the behavior predicted if $d^2/s^2 < 1/2$.

PM and PS have $d^2/s^2 < 1/2$. As Re_x grows to exceed Re_W, the local drag coefficient switches from blend formula (78) to smooth formula (79). The Re_W formula (50) transitions are marked by arrows.

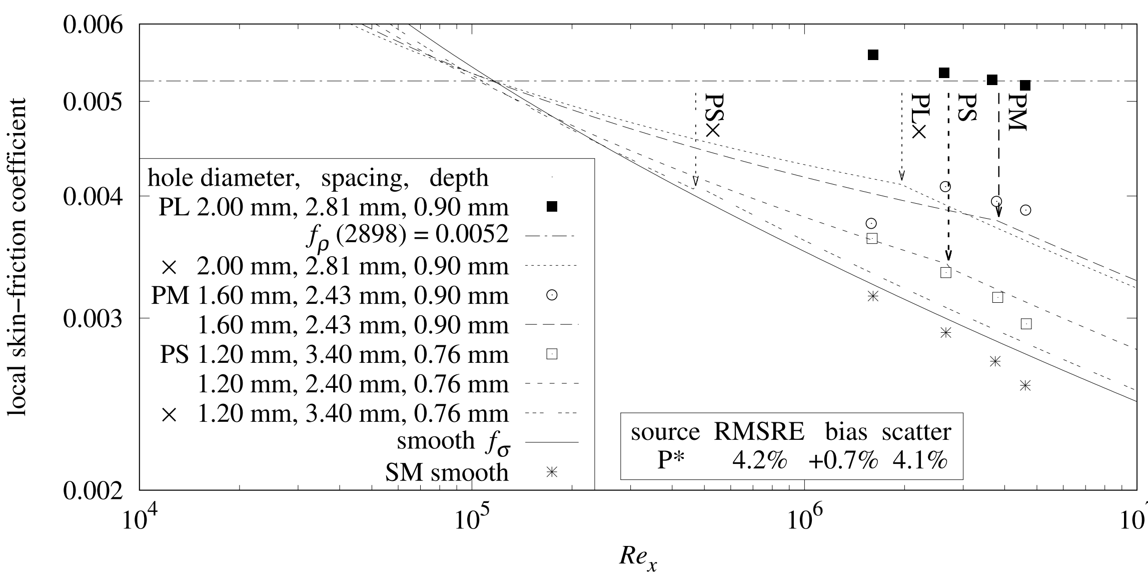

Figure 26 local f_ρ versus Re_x of perforated sheet

PL and PM measurements match the present theory within the ±9% measurement uncertainty. The PS measurements do not match unless a hypothesized single digit misprint in [14] is corrected, changing the PS hole spacing from 3.4 mm to 2.4 mm. The "PS×" trace shows the behavior predicted of the original PS. Taken together, the three (corrected) perforated plates have 4.2% RMSRE versus the present theory.

The non-horizontal traces for PM and PS show they lack constant terminal drag coefficients.

23. **Forced convection measurements**

Both the Pimenta et al [7] and Bergstrom et al [14] measurements are restricted to flow rate ranges of less than 3:1. For a novel theory to be persuasive, confirmations over a wider range of flow rates are needed.

The present apparatus combined an open intake wind-tunnel, digital phase-locked fan control, and a heated bi-level aluminum plate having $\varepsilon = 3.0$ mm. This combination measured average convection in air at $2300 < Re < 87400$, a 38:1 range. Section 29 describes the apparatus and measurement methodology.

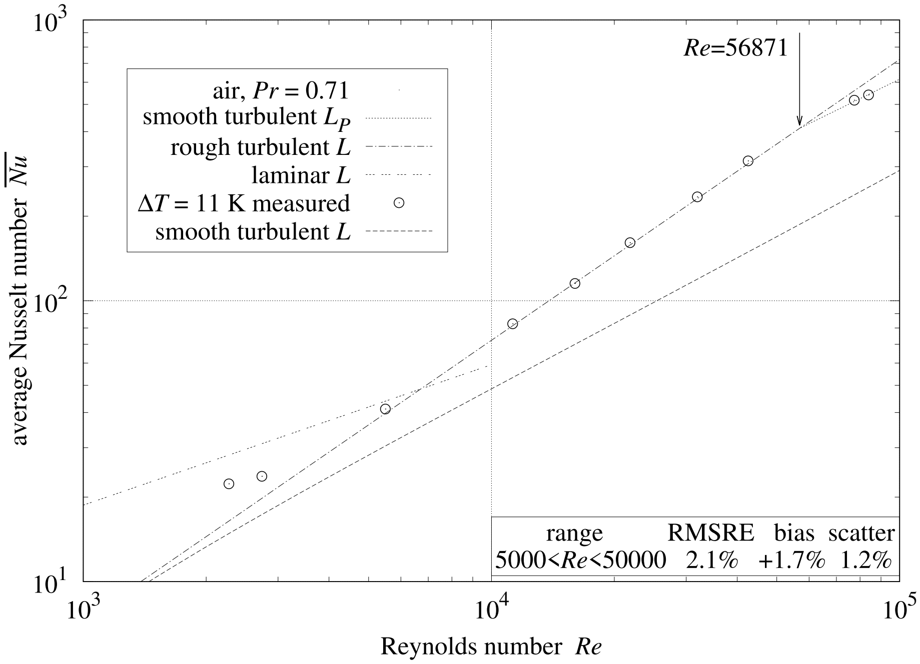

Figure 27 convection from bi-level plate; $L/\varepsilon = 305/3$

The $L/\varepsilon \approx 101$ ratio corresponds to a relative sand-roughness of $L/k_S \approx 19$.

With such a rough plate, the two edges of the bi-level plate roughness which are parallel to the fluid flow also contribute to forced convection, increasing the effective width of the bi-level plate by $4\,\varepsilon$ (1.4%). Applying the average convection formula (61) to the bi-level plate geometry (with the 1.4% correction) yields:

$$\overline{Nu} = 0.00811\,Re\,Pr^{1/3} \tag{82}$$

In Figure 27, the points labeled "$\Delta T = 11\,\mathrm{K}$ measured" are the $\overline{Nu}$ measurements with the plate averaging 11 K warmer than the ambient air. At $Re < 5000$, the natural convection component dominates the mixture of natural and forced convection. The "rough turbulent L" trace in Figure 27 is equation (82); the "measured" points match it with 2.1% RMSRE in the range $5000 < Re < 50000$. At $Re > 55000$ the "smooth turbulent L_P" trace is formula (76); its 4/5 slope shows that convection is from a smooth turbulent flow. Its height above the "smooth turbulent L" trace shows that it is operating with a shorter characteristic-length than "smooth turbulent L". Re_I equation (48) calculates that the transition from "rough turbulent L" to "smooth turbulent L_P" is at $Re_I \approx 56871$, which is marked with an arrow in Figure 27.

Re_λ formula (42) predicts that the flow along the entire bi-level plate transitions from laminar to rough turbulence at $Re_\lambda \approx 175$, which is too slow to test in this apparatus. However, a 1 mm roughness plate with $Re_\lambda \approx 1238$ was tested in the wind-tunnel and found to be rough turbulent at $Re \approx 2300$, which is within a factor of 2 of its predicted Re_λ transition.

The periodic bi-level plate behaving compatibly with formula (61) supports the assertion that formulas (28) and (61) are intrinsic to turbulent flow along isotropic roughness.

A constant terminal drag coefficient corresponds to asymptotic $\overline{Nu} \propto Re$. The transition to smooth turbulence at $Re_I \approx 56871$ shows that this plateaued plate lacks a constant terminal drag coefficient.

24. **Cloth tape**

The bi-level test plate of the present apparatus has four sides perpendicular to the test surface, each a wedge of extruded polystyrene foam (XPS) insulation filling a 2.7 cm 45° chamfer in the metal slab. In order to isolate the convective heat flow of the test surface from that of the sides, the estimated side convection, about 10% of total, is deducted from the measured heat flow (see Section 29 for details).

Figure 28 XPS foam board

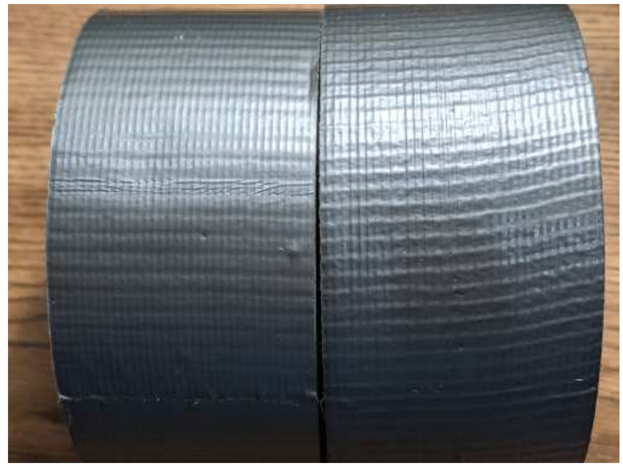

Figure 29 rolls of cloth tape

The surface of the XPS foam board in Figure 28 was not smooth and not an isotropic, periodic roughness. Without a theoretical basis for computing its convection, the accuracy of measurements of the rough surface would have been quite limited.

The cloth tape shown in Figure 29 is a thread mesh in adhesive on a thin plastic sheet. The vertical periods are longer than the horizontal periods. Using woven wire mesh formula (80) with the geometric mean of the spatial periods as $s \equiv L_P$, the thread diameter plus the sheet thickness as d, and $L = 0.305$ m yields Tables 8 and 9; Table 9 is identical to the "cloth tape" rows in Table 2.

	thread cell	$s \equiv L_P$	d	ε
cloth tape (dull)	3.62 mm×1.47 mm	2.31 mm	0.10 mm	0.0431 mm
cloth tape (shiny)	3.05 mm×1.29 mm	1.98 mm	0.09 mm	0.0346 mm

Table 8 cloth tape dimensions

	L/L_P	L/ε	$L/\sqrt{\varepsilon\, L_P}$		Re_σ		Re_λ
cloth tape (dull)	1.32×10^2	8.82×10^3	1.08×10^3	$<$	6.70×10^3	$\ll$	2.59×10^5
cloth tape (shiny)	1.54×10^2	7.08×10^3	1.04×10^3	$<$	2.49×10^3	$\ll$	1.43×10^5

Table 9 cloth tape parameters

An $L = 0.305$ m strip of either tape fails to generate rough turbulence because the apparatus's largest $Re \approx 87400 < Re_\lambda$. Both tapes have $L/\sqrt{\varepsilon\, L_P} < Re_\sigma$, for which the present theory predicts rough laminar formula (74) convection.

With cloth tape applied to the foam faces, the measurements presented in Section 23 are consistent with the side convection modeled by rough laminar formula (74). The other curves in Figure 20 are substantially less than formula (74), and do not account for enough heat transfer to keep the surface-under-test measurements within the expected uncertainty bounds presented in Section 29.

Representing only about 10% of the forced convective heat flow from the plate assembly, this evidence is not conclusive for rough laminar formula (74); but it does support the assertion that (forced) laminar convection from a rough surface is larger than either laminar or turbulent convection from a smooth surface of the same size.

25. **Discussion**

Rather than trying to tease rough turbulence from a nearly smooth surface, this investigation started its analysis with roughness thicker than smooth plate viscous sub-layers. Recapitulating the development:

- Self-similar roughness repeatedly disrupts emerging boundary-layers along a plate.
- Self-similar roughness has a constant characteristic-length per RMS height-of-roughness ratio $L/\varepsilon \gg 1$ at a succession of scales converging to 0. This leads to friction velocity $u_\tau = u/[\sqrt{3}\,\ln(L/\varepsilon)]$.
- Plate surfaces with isotropic self-similar roughness have skin-friction coefficient: $\overline{f_\rho} = [1/3]\,\ln^{-2}(L/\varepsilon)$.
- Consideration of roughness Reynolds number $Re_\varepsilon = 1$ leads to a formula for turbulent average skin-friction coefficient from a smooth plate: $\overline{f_\sigma} = \left[\sqrt[3]{2}/3\right]\left[\mathrm{W}_0\left(Re/\sqrt{3}\right) - 1\right]^{-2}$. Measurements from Smith and Walker [20] and Spalding and Chi [21] compiled by Churchill [11] match $\overline{f_\sigma}$ with 0.75% RMSRE.
- The discrete Fourier transform of elevations from a square portion of a rough surface can be used to determine the isotropic spatial period L_P and openness Ω of that roughness.
- The transition from laminar or smooth turbulent flow to rough turbulent flow along a plate with isotropic, periodic roughness occurs when ε exceeds the larger of the smooth turbulent or laminar momentum thicknesses of a smooth plate at $x = L_P$. Measurements from the present apparatus support $Re_\lambda = [0.664/\varepsilon]^2\,L_P\,L$ as the rough turbulent lower-bound within a factor of 2.
- Flow along plateau roughness ($\Omega < 1/2$) can transition from rough to smooth turbulent flow with increasing Re_x. Both plateau islands and wells were successfully modeled and tested.
- Flow will be rough turbulent along the entire surface when $\Omega > 1/2$ and $Re > \max(Re_\sigma, Re_\lambda)$.
- Converting between local and average skin-friction coefficients differs for flows having continuous versus disrupted boundary-layers. Transforms in both directions were presented and used to compare prior work with present work.
- Rough turbulent forced convection is: $\overline{Nu_\rho} = Re\,Pr^{1/3}/[6\,\ln^2(L/\varepsilon)]$. Bi-level plate experiments by the author match this formula with 2.1% RMSRE over the range $5000 < Re < 50000$.
- The similarity of forced convection to natural convection from a vertical plate leads to a formula for smooth turbulent average forced convection. This formula matches the (averaged) turbulent formula from Lienhard [24] within ±6.6% over $10^5 < Re < 4.3 \times 10^6$ with $4.0 \le Pr \le 257$.
- Over the range $Re < Re_\lambda$, an isotropic, periodic plate can be treated as smooth if $L/\sqrt{\varepsilon\,L_P} > Re_\sigma$. Otherwise, laminar convection from a rough plate is $\|\overline{Nu_\lambda}(Re), \overline{Nu_\sigma}(Re)\|_{\sqrt{2}}$ over the range $Re < Re_\lambda$.
- Measurements of local skin-friction coefficient versus x/ε and Re_x from the Pimenta et al sphere-roughened plate match predictions of the present theory with 4.5% RMSRE.
- Experiments with the isotropic, periodic roughness of bi-level, sphere-roughened, mesh-covered, and perforated plates find that convection and skin-friction coefficients are close to the present theory formulas with Re as small as 5000 and as large as 5×10^6.

All of the plateau roughness measurements cited or performed by this investigation were from plates with bi-level roughness.

The Colburn [28] analogies relate friction factors to forced convective heat transfer. For laminar flow:

$$\overline{Nu} = \frac{\overline{f_c}}{2}\,Re\,Pr^{1/3} \tag{83}$$

Combining equation (83) with rough $\overline{f_\rho}$ equation (28) results in $\overline{Nu_\rho} = Re\,Pr^{1/3}/[6\,\ln^2(L/\varepsilon)]$, which is identical to rough turbulent convection equation (61).

Thus, the Pr dependence of laminar and rough turbulent convection are both $Pr^{1/3}$, while it is more complicated in smooth turbulent convection formula (70).

26. Conclusions

- The turbulence induced in a steady flow of strength Re along a flat, smooth plate has average (not local) skin-friction coefficient $\overline{f_\sigma}$, average forced convection $\overline{Nu_\sigma}$, and local momentum thickness δ_2:

$$\overline{f_\sigma} = \frac{\sqrt[3]{2}/3}{\left[\mathrm{W}_0\left(Re/\sqrt{3}\right) - 1\right]^2} \qquad \overline{Nu_\sigma} = \frac{Nu_0\,Re}{\sqrt{3}}\sqrt{\frac{\overline{f_\sigma}\;\left[Pr/\sqrt{162}+1\right]}{\sqrt{162}\,Pr + 1/\,\overline{f_\sigma}}}\;\sqrt[3]{\frac{Pr/\Xi(Pr)}{\|1, 1/Pr\|_3}}$$

$$\delta_2 = \frac{x}{3^3\;\mathrm{W}_0\left(Re_x/\sqrt{3}\right)} \qquad Re_x = \frac{x}{L}\,Re \qquad \sqrt{3}\,\mathrm{e} < Re_x \le Re \qquad Re \gg \sqrt{3}\,\mathrm{e}$$

$$Nu_0 = \frac{16}{\pi^2\,\sqrt[4]{2}} \qquad \Xi(Pr) = \left\|1,\ \frac{0.5}{Pr}\right\|_{\sqrt{1/3}} \qquad \|\varphi,\vartheta\|_p \equiv \left(|\varphi|^p + |\vartheta|^p\right)^{1/p}$$

where W_0 is the principal branch of the Lambert W function: $\mathrm{W}_0(\varphi\exp\varphi) = \varphi$ when $\varphi \ge 0$.

Section 14 derived local skin-friction coefficients $f_\sigma(Re_x)$ and $f_\rho(x/\varepsilon)$.

- Periodicity combined with isotropy enables modeling of flows along many plate roughness geometries using few parameters: characteristic-length L, RMS height-of-roughness ε, isotropic spatial period L_P, openness Ω, and, for plateau roughness, convex region L^*.
- Algorithms presented find ε, L_P, and Ω from an elevation grid of a square portion of the rough surface.
- A plate surface is isotropic, periodic roughness when its $L/L_P \gg 1$.

The following conclusions are for plate surfaces with $L/L_P \gg 1$.

- The average skin-friction coefficient $\overline{f_\rho}$ and average forced convection $\overline{Nu_\rho}$ for rough turbulence are:

$$\overline{f_\rho} = \frac{1}{3\,\ln^2(L/\varepsilon)} \qquad \overline{Nu_\rho} = \frac{Re\,Pr^{1/3}}{6\,\ln^2(L/\varepsilon)} \qquad \frac{L}{\varepsilon} \gg 1$$

- Fluid flow will be rough turbulent in the leading band of roughness when $Re > \max(Re_\sigma, Re_\lambda)$:

$$Re_\sigma = \frac{\sqrt{3}\,L}{3^3\,\varepsilon}\exp\frac{L_P}{3^3\,\varepsilon} \qquad Re_\lambda = \left[\frac{0.664}{\varepsilon}\right]^2 L_P\,L$$

- Fluid flow will be rough turbulent along the entire surface when $\Omega > 1/2$ and $Re > \max(Re_\sigma, Re_\lambda)$.

The following conclusions are for plate surfaces with $Re_\sigma < Re_\lambda$ and $L/L_P \gg 1$.

- When $Re < Re_\lambda$, a roughness with $L/\sqrt{\varepsilon\,L_P} > Re_\sigma$ behaves as a smooth surface.
- When $Re < Re_\lambda$, a roughness with $L/\sqrt{\varepsilon\,L_P} < Re_\sigma$ has average forced convection:

$$\overline{Nu}(Re) = \left\|\overline{Nu_\lambda}(Re), \overline{Nu_\sigma}(Re)\right\|_{\sqrt{2}} \qquad \overline{Nu_\lambda} = 0.664\,\sqrt{Re}\,Pr^{1/3}$$

- A plateau islands roughness with $\Omega < 1/2$ and $Re > Re_\lambda$ has average forced convection:

$$\overline{Nu} = \begin{cases} \overline{Nu_\rho}(Re), & \text{if } [4\,L^*]^2/L_P^2 < 1/2;\\ \overline{Nu_\rho}(Re), & \text{if } Re \le Re_I;\\ \overline{Nu_\rho}(Re_I) + \overline{Nu_I}(Re) - \overline{Nu_I}(Re_I), & \text{otherwise.}\end{cases}$$

$$Re_I = \frac{3^3\,\varepsilon^2\,L^2}{L^*\,L_P^3}\,\ln\frac{3^3\,\varepsilon^2\,L^2}{\sqrt{3}\,L^*\,L_P^3}$$

$$\overline{Nu_I}(Re) = \left[1 - \Omega + \left\|\frac{\Omega}{2}, \frac{2\,\varepsilon\,[4\,L^*]}{L_P^2}\right\|_2\right]\frac{L}{L_P}\,\overline{Nu_\sigma}\left(\frac{Re\,L_P}{L}\right)$$

- A plateau wells roughness with $\Omega < 1/2$ and $Re > Re_\lambda$ has local skin-friction coefficient:

$$f_c = \begin{cases} \overline{f_\rho}(L/\varepsilon), & \text{if } [4\,L^*]^2/L_P^2 > 1/2;\\ \Omega\,\overline{f_\rho}(L/\varepsilon) + [1-\Omega]\,f_\sigma(Re_x), & \text{if } Re_x \le Re_W;\\ \left\|1, 2\,\pi\,\varepsilon\,[4\,L^*]/L_P^2\right\|_{\sqrt[4]{8}}\,f_\sigma(Re_x), & \text{otherwise.}\end{cases}$$

$$Re_W = \frac{3^3\,\varepsilon^2\,L^2}{2^3\,L^*\,L_P^3}\,\ln\frac{3^3\,\varepsilon^2\,L^2}{2^3\,\sqrt{3}\,L^*\,L_P^3}$$

27. Nomenclature

A = rough plate area (m^2)
$c_f, \overline{c_f}$ = local, average skin-friction coefficient Prandtl-Schlichting [3]
$C_f/2, \overline{C_f}/2$ = local, average skin-friction coefficient Mills-Hang [8] and Pimenta et al [7]
$C_m/2$ = average skin-friction coefficient Churchill [11]
$f_c, \overline{f_c}$ = local, average skin-friction coefficient present work
$G(t,w)$ = Gray-code self-similar ramp-permutation
j_P = period index, the index of largest $|X_j|$ or $|X_{j,k}|$
k_S = sand-roughness (m)
L = plate characteristic-length (m)
L_P = roughness spatial period (m)
L^* = ratio of plateau convex region area to its perimeter (m)
n = branching factor of profile roughness function
$Nu, \overline{Nu}$ = local, average Nusselt number (convection)
Pr = Prandtl number of fluid
$q = \log_2 w$ = positive integer
Re = Reynolds number of flow parallel to the plate
Re_I, Re_W = Re_x rough-to-smooth turbulence threshold
Re_λ, Re_σ = laminar, smooth turbulent Re upper-bound
$Re_\varepsilon = u_\tau\,\varepsilon/\nu, Re_k = u_\tau\,k_S/\nu$ = roughness, sand-roughness Reynolds number
$Re_x = x\,Re/L$ = local Reynolds number
Re_0 = Re_x integration lower bound
$S_{j,k}$ = matrix of elevations
t = integer
u, u_τ = bulk fluid, friction velocity (m/s)
$w = 2^q$ = integer power of two
$W(t,w)$ = wiggliest integer self-similar ramp-permutation
W_0 = principal branch of the Lambert W function
x = distance from leading edge of plate (m)
$X_j, X_{j,k}$ = discrete Fourier transform coefficient
$Y(t,w)$ = integer self-similar ramp-permutation
z = roughness function (m)
$\overline{z}$ = mean elevation of roughness function (m)
Z = roughness random variable (m)

Greek Symbols

δ_2 = momentum thickness of boundary-layer flow (m)
$\delta_{2\lambda}, \delta_{2\sigma}$ = laminar, smooth turbulence momentum thickness (m)
ϵ, ε = profile, surface RMS height-of-roughness (m)
ν = fluid kinematic viscosity (m^2/s)
Ω = ratio of non-plateau area to cell area ($\mathrm{m}^2/\mathrm{m}^2$)
ρ = fluid density ($\mathrm{kg/m}^3$)
τ, τ_2 = fluid shearing stress ($\mathrm{N/m}^2$)
ς = peak elevation of roughness (m)
φ, ϑ = mathematical scalar variables

Acknowledgments

The idea of self-similar roughness grew from a discussion with Nina Koch about turbulence self-similarity. Thanks to John Cox (1957-2022) and Doug Ruuska for machining the bi-level plate. Thanks to Martin Jaffer for critiques and insights. Thanks to anonymous reviewers for their useful suggestions.

28. References

[1] L Prandtl. Zur turbulenten stromüng in rohren und längs platten. *Ergebnisse der Aerodynamische Versuchsanst zu Göttingen*, 4:18–29, 1932.

[2] T. von Kármán. Theorie des reibungswiderstandes [theory of the frictional resistance]. In *Hydromechanische Probleme des Schiffsantriebs*, pages 50–73, Hamburg, Germany, 1932. Springer.

[3] L. Prandtl and H. Schlichting. *The Resistance Law for Rough Plates*. Translation (David W. Taylor Model Basin). Navy Department, the David W. Taylor Model Basin, 1934. Translated 1955 by P.S. Granville.

[4] J. Nikuradse. Laws of flow in rough pipes. *VDI Forschungsheft*, page 361, 1933. Translated 1937 by A. A. Brielmaier.

[5] H Schlichting. Experimental investigation of the problem of surface roughness. Technical Report TM 823, NACA, Washington, DC, 1937.

[6] F. R. Hama. Boundary layer characteristics for smooth and rough surfaces. *Trans. Soc. Nav. Arch. Marine Engrs.*, 62:333–358, 1954.

[7] M. M. Pimenta, R. J. Moffat, and W. M. Kays. *The Turbulent Boundary Layer: An Experimental Study of the Transport of Momentum and Heat with the Effect of Roughness*. Department of Mechanical Engineering, Stanford University, 1975.

[8] A. F. Mills and Xu Hang. On the skin friction coefficient for a fully rough flat plate. *J. Fluids Eng*, 105(3):364–365, 1983.

[9] Hermann Schlichting, Klaus Gersten, Egon Collaborateur. Krause, Herbert Collaborateur. Oertel, and Katherine Mayes. *Boundary-layer theory*. Springer, Berlin, Heidelberg, Paris, 2000. Corrected printing 2003.

[10] Frank White. *Viscous Fluid Flow, 3rd Edition*. McGraw-Hill, 2006.

[11] Stuart W. Churchill. Theoretically based expressions in closed form for the local and mean coefficients of skin friction in fully turbulent flow along smooth and rough plates. *International Journal of Heat and Fluid Flow*, 14(3):231 – 239, 1993.

[12] C. F. Colebrook. Turbulent flow in pipes, with particular reference to the transition region between the smooth and rough pipe laws. *Journal of the Institution of Civil Engineers*, 11(4):133–156, 1939.

[13] Javier Jiménez. Turbulent flows over rough walls. *Annual Review of Fluid Mechanics*, 36(1):173–196, 2004.

[14] D. J. Bergstrom, O. G. Akinlade, and M. F. Tachie. Skin Friction Correlation for Smooth and Rough Wall Turbulent Boundary Layers. *Journal of Fluids Engineering*, 127(6):1146–1153, 04 2005.

[15] Mark F. Tachie, D. J. Bergstrom, Ram Balachandar, and Shyam Ramachandran. Skin Friction Correlation in Open Channel Boundary Layers . *Journal of Fluids Engineering*, 123(4):953–956, 05 2001.

[16] Noor Afzal, Abu Seena, and A. Bushra. Turbulent flow in a machine honed rough pipe for large reynolds numbers: General roughness scaling laws. *Journal of Hydro-environment Research*, 7(1):81–90, 2013.

[17] Karen A Flack, Michael P Schultz, Julio M Barros, and Yechan C Kim. Skin-friction behavior in the transitionally-rough regime. *International Journal of Heat and Fluid Flow*, 61:21–30, 2016.

[18] J. H. Lienhard, IV and J. H. Lienhard, V. *A Heat Transfer Textbook*. Phlogiston Press, Cambridge, MA, 5th edition, August 2020. Version 5.10.

[19] Mitchell G. Newberry and Van M. Savage. Self-similar processes follow a power law in discrete logarithmic space. *Phys. Rev. Lett.*, 122:158303, Apr 2019.

[20] D. W. Smith and J. D. Walker. Skin friction measurements in incompressible flow. Technical Report R-26, NASA, Washington, DC, 1959.

[21] D. B. Spalding and S. W. Chi. The drag of a compressible turbulent boundary layer on a smooth flat plate with and without heat transfer. *Journal of Fluid Mechanics*, 18(1):117143, 1964.

[22] RJ Goldstein, EM Sparrow, and DC Jones. Natural convection mass transfer adjacent to horizontal plates. *International Journal of Heat and Mass Transfer*, 16(5):1025–1035, 1973.

[23] JR Lloyd and WR Moran. Natural convection adjacent to horizontal surface of various planforms. *Journal of Heat Transfer*, 96(4):443–447, 1974.

[24] V Lienhard, John H. Heat Transfer in Flat-Plate Boundary Layers: A Correlation for Laminar, Transitional, and Turbulent Flow. *Journal of Heat Transfer*, 142(6), 04 2020. 061805.

[25] Aubrey Jaffer. Natural convection heat transfer from an isothermal plate. *ArXiv e-prints*, 2022.

[26] E. O. Tuck and A. Kouzoubov. A laminar roughness boundary condition. *Journal of Fluid Mechanics*, 300:5970, 1995.

[27] S. W. Churchill and R. Usagi. A general expression for the correlation of rates of transfer and other phenomena. *AIChE Journal*, 18(6):1121–1128, 1972.

[28] Allan P. Colburn. A method of correlating forced convection heat-transfer data and a comparison with fluid friction. *International Journal of Heat and Mass Transfer*, 7(12):1359 – 1384, 1964.

[29] Rice R.W. Emittance factors for infrared thermometers used for wood products. *Wood and Fiber Science*, 36:520–526, 2004.

[30] Eva Barreira, Ricardo M. S. F. Almeida, and Maria L. Simes. Emissivity of building materials for infrared measurements. *Sensors*, 21(6), 2021.

[31] R.B. Abernethy, R.P. Benedict, and R.B. Dowdell. Asme measurement uncertainty. *ASME. J. Fluids Eng.*, 107(2):161–164, 1985.

29. Appendix: convection measurement apparatus and methodology

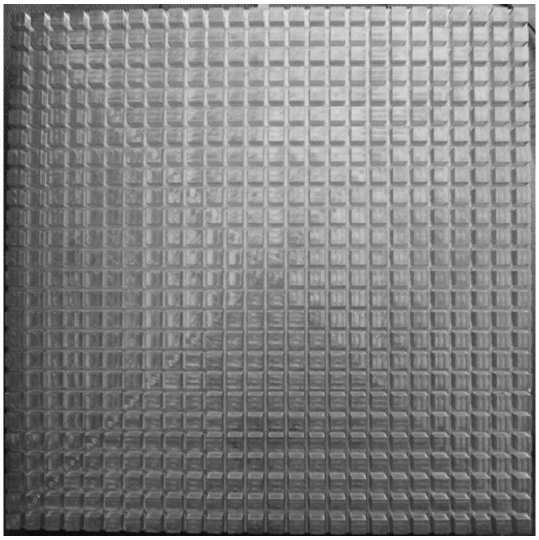

Figure 30 **rough surface of plate**

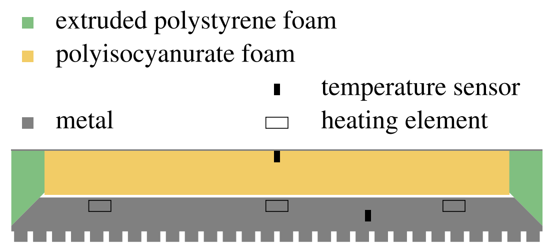

Figure 31 **cross-section of plate assembly**

The goal was to measure forced convection from a rough plate over the widest practical span of Re.

Figure 30 shows the rough surface of the test plate; it was milled from a slab of MIC-6 aluminum to have (676 of) square $8.5\,\text{mm} \times 8.5\,\text{mm} \times 6\,\text{mm}$ posts spaced on 11.7 mm centers over the 30.5 cm × 30.5 cm plate. The area of the top of each post was $0.722\,\text{cm}^2$, which was 53% of its $1.37\,\text{cm}^2$ cell. The RMS height-of-roughness $\varepsilon = 3.00$ mm. Openness $\Omega \approx 47\%$. Embedded in the plate are 9 electronic resistors as heating elements and an LM35 temperature sensor. 2.54 cm of thermal insulating foam separates the back of the plate from a 0.32 mm thick sheet of aluminum with an LM35 temperature sensor at its center. Figure 31 is a cross-section illustration of the plate assembly.

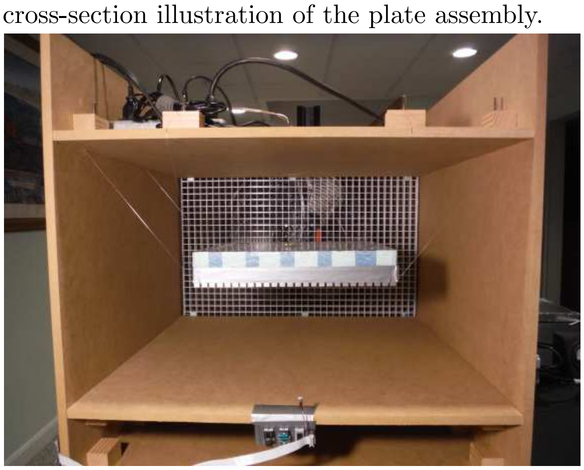

Figure 32 $\varepsilon = 3$ mm **plate in wind-tunnel**

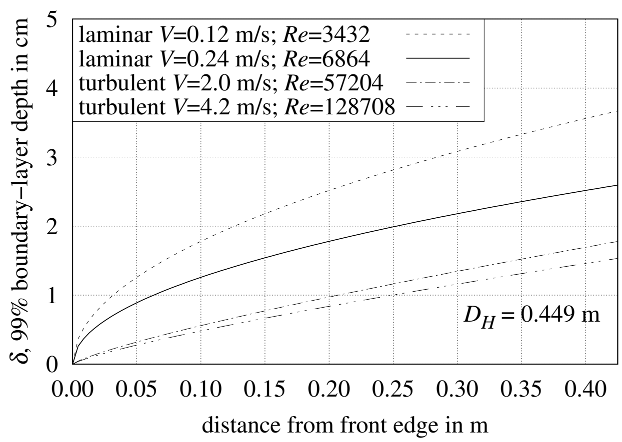

Figure 33 **wind-tunnel boundary-layers**

In order to guarantee isobaric flow, the wind-tunnel must be large enough that the boundary-layers of the test chamber and plate assembly do not interact.

The wind-tunnel test chamber in Figure 32 has a 61 cm × 35.6 cm cross-section and a 61 cm depth. This allows the plate assembly to be centered in the wind-tunnel with 15 cm of space on all sides. The fan pulling air through the test chamber produces a maximum airspeed of 4.25 m/s ($Re \approx 9 \times 10^4$ along the 30.5 cm square plate). Its minimum nonzero airspeed is 0.12 m/s ($Re \approx 2300$).

The wind-tunnel laminar and smooth turbulent 99% boundary-layer thicknesses (Schlichting [9]) are:

$$\delta_\lambda = 4.92\sqrt{\frac{x\nu}{u}} \qquad \delta_\sigma = 0.37\,x^{4/5}\left(\frac{\nu}{u}\right)^{1/5} \tag{84}$$

Figure 33 shows that the 15 cm clearance between the plate and the test chamber walls is sufficient to prevent their boundary-layers from interacting at airspeeds within the fan's capabilities.

Rotations of the fan impeller are sensed when a fan blade interrupts an infrared beam. A microprocessor controls a solid-state relay (supplying power to the fan) to maintain a fan rotation rate, ω, which is dialed into switches. At $\omega < 400$ r/min, the microprocessor pulses power to the fan to phase-lock the beam interruption signal to an internal clock. At $\omega > 400$ r/min, the microprocessor servos the duty cycle of a 10 Hz square-wave which gates power to the fan. This system operates stably at 32 r/min $< \omega <$ 1500 r/min.

The correspondence between the fan rotation rate ω and the airspeed u near the center of the empty test chamber was determined using the "ABM-200 Airflow & Environmental Meter" anemometer, which specifies an accuracy of ±0.5% of reading between 2.2 m/s and 62.5 m/s.

Spinning the fan impeller faster eventually yields diminishing returns of airspeed. The solid line in Figure 34 is formula (85) with airspeed upper-bound $u_u = 7.5$ m/s. With 500 r/min $\le \omega \le$ 1500 r/min, $u(\omega)$ has 0.3% RMSRE versus the mean of four anemometer readings per ω value.

$$u(\omega) = \left[\left[\frac{\omega}{1500 \text{ r/min}}\right]^{-2} \left[u_{1500}^{-2} - u_u^{-2}\right] + u_u^{-2}\right]^{-1/2} \qquad u_{1500} \approx 4.172 \text{ m/s} \tag{85}$$

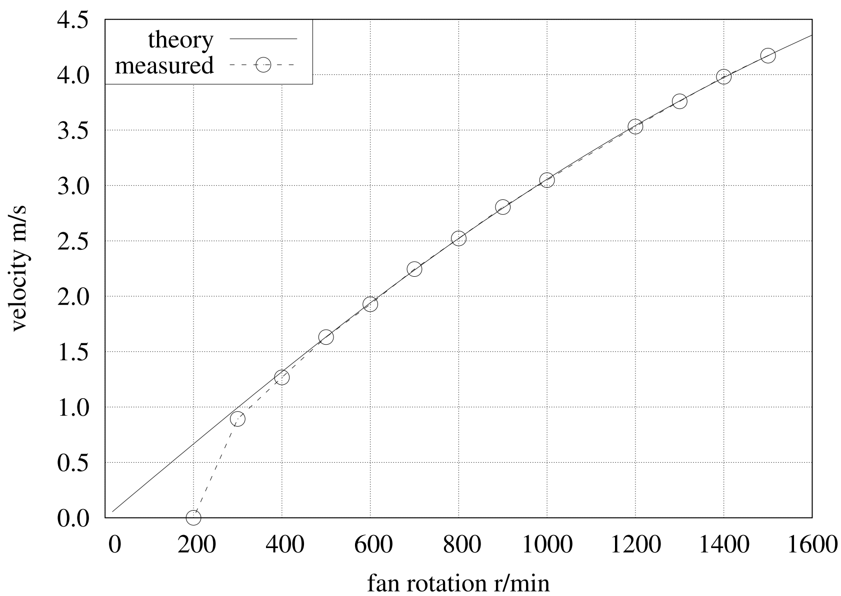

Figure 34 airspeed vs fan rotation

The plate assembly is suspended from four lengths of 0.38 mm-diameter steel piano wire, which are terminated at eight zither tuning pins in wooden blocks fastened to the outside of the test chamber. The wire is sheathed by 0.95 mm Teflon tubing where it would otherwise contact the plate metal.

The plate is suspended face down to minimize the natural convection from the test surface.

With the plate assembly in the test chamber, the airspeed increases in proportion to the reduction of test chamber aperture A_e by the plate's cross-sectional area $A_\times$:

$$\frac{u'}{u} = \frac{A_e}{A_e - A_\times} \approx 107.7\% \tag{86}$$

Data capture and control of convection experiments are performed by an "STM32F3 Discovery 32-Bit ARM M4 72MHz" development board. The program written for the STM32F3 captures readings and writes them to the microprocessor's non-volatile RAM, controls the plate heating, servos the fan speed, and (later) uploads the captured data to a laptop computer over a USB cable. Once per second during an experiment, the program calibrates and reads each on-chip 12 bit analog-to-digital converter 16 times, summing the sixteen 12 bit readings to create a 16 bit reading per converter.

Figure 35 shows the ambient sensor board which is at the lower edge of the tunnel in Figure 32. It measures the pressure, humidity, and temperature of the air at the wind-tunnel intake. The LM35 temperature sensor projects into the tunnel; it is wrapped in aluminum tape to minimize radiative heat transfer. To minimize self-heating, it is necessary to power the LM35 only while it is being sampled.

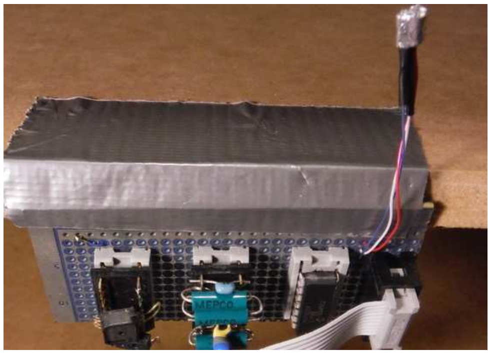

Figure 35 ambient sensors

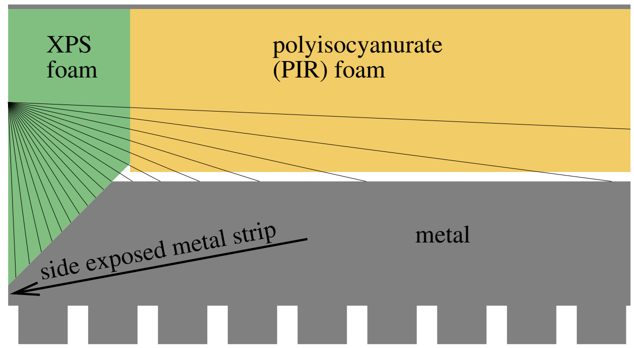

Figure 36 XPS wedge conduction

The measurement methodology employed is unusual. Instead of waiting until the plate reaches thermal equilibrium, the plate is heated to 15 K above ambient, heating stops, the fan is started, and the sensor readings are captured every second of 102 minutes as convection cools the plate.

The static physical parameters from measurements and material specifications are:

L	0.305 m	length of test plate
ε	3.0 mm	RMS height-of-roughness
A	0.093 m^2	area of test plate
D_{Al}	19.4 mm	metal slab thickness
D_{PIR}	25.4 mm	polyisocyanurate foam thickness
C_{pt}	4690 J/K	plate thermal capacity
k_{PIR}	0.023 $\mathrm{W/(m \cdot K)}$	polyisocyanurate foam thermal conductivity
k_{XPS}	0.033 $\mathrm{W/(m \cdot K)}$	extruded polystyrene foam thermal conductivity
U_I	0.075 W/K	composite insulation thermal conductance
ϵ_{es}	0.71	effective side emissivity (see text)
ϵ_{rs}	0.04	rough surface (MIC-6) emissivity
ϵ_{wt}	0.90	test chamber emissivity

Table 10 physical parameters

MIC-6 aluminum was chosen for its low emissivity, $\epsilon_{rs} = 0.04$. The radiative heat loss from the rough face of the plate is only 20 mW/K, which is about 2% of the 1.08 W/K expected from $u = 1$ m/s convection.

The effective ϵ_{wt} may differ from the medium-density-fiberboard emissivity given by Rice [29] because the temperatures of the test chamber surfaces may not be uniform. Through the open intake, the plate also exchanges thermal radiation with objects in the room having different temperatures.

Figure 32 shows that cloth tape was applied to the lower half of the XPS foam wedges. Barreira, Almeida, and Simões [30] measured emissivities of 0.86 and 0.89 from two brands of "duct tape". Emissivity measurements from XPS foam could not be found.

Natural convection ($u = 0$) is more sensitive to ϵ_{es} than with $u > 0$. When $\epsilon_{es} = 0.71$, natural convection over the span of plate inclinations has RMSRE$<$ 2%; RMSRE$>$ 2% when $\epsilon_{es} < 0.705$ or $\epsilon_{es} > 0.715$. The area proportional mean of cloth tape emissivity (0.875) and XPS emissivity is ϵ_{es}; solving it for XPS emissivity yields 0.53, which is consistent with convection measurements from the plate assembly without tape.

The dynamic physical quantities which are measured every second are:

u	m/s	air velocity (from the fan rotation rate)
T_P	K	plate temperature
T_F	K	air temperature
T_B	K	back surface temperature
P	Pa	atmospheric pressure
Φ	Pa/Pa	air relative humidity

Table 11 dynamic quantities

Table 12 lists computed quantities. $U_S(u)$ and $\epsilon_{rs}\,\epsilon_{wt}\,h_R\,A$ are discounted from the combined heat flow. The mean of $\overline{h}(u,t)$ over the time interval in which ΔT drops by half is the result from that experiment.

h_R	W/(m^{2}K)	radiative surface conductance
$U_S(u)$	W/K	side radiative and convective conductance
$\overline{h}(u,t)$	W/(m^{2}K)	convective surface conductance

Table 12 computed quantities

The four sides are not isothermal; each has an exposed 3.5 mm metal strip (see cross-section Figure 36) running the length of the side, and a wedge of extruded polystyrene foam (XPS) insulation filling the 27 mm ($= \sqrt{2}\, D_{\rm Al}$) 45° chamfer. The local surface conductance $h_W(z)$ at elevation z (from the wedge point) is found by integrating the reciprocal distance to slab metal with respect to angle θ:

$$\begin{aligned} h_W(z) &= \frac{k_{\rm XPS}}{\sqrt{2}\, z} \int_0^{\theta_c} \cos\left(\theta + \frac{\pi}{4}\right) \mathrm{d}\theta + \frac{k_{\rm PIR}}{z - D_{\rm Al}} \int_{\theta_w}^{\theta_W} \cos\theta \, \mathrm{d}\theta \\ &= \frac{k_{\rm XPS}}{\sqrt{2}\, z} \left[\sin\left(\theta_c + \frac{\pi}{4}\right) - \sin\frac{\pi}{4}\right] + \frac{k_{\rm PIR}}{z - D_{\rm Al}} \left[\sin\theta_W - \sin\theta_w\right] \end{aligned} \tag{87}$$

$$\theta_c = \arctan \frac{D_{\rm Al} - z}{D_{\rm Al}} \quad \theta_w = \arctan\frac{D_{\rm Al}}{z - D_{\rm Al}} \quad \theta_W = \max\left(\theta_w,\ \arctan\frac{L - D_{\rm Al}}{z - D_{\rm Al}}\right)$$

Forced air flows parallel to the long dimension on two sides, but flows into the windward side and away from the leeward side. Air heated by the windward side reduces heat transfer from the test surface; air heated by the test surface suppresses heat transfer from the leeward side. Hence, the model excludes windward and leeward forced convection. The forced convective conductance of the flow-parallel foam wedges is calculated by integrating $h_W(z)$ in series (reciprocal of the sum of reciprocals, the ℓ^{-1}-norm) with the local surface conductance $k\, Nu(Re_x)/L$, where $Nu(Re_x)$ is the rough laminar convection calculated by applying $\overline{Nu_\sigma} \to Nu_\sigma$ transform (72) to the rough laminar convection formula (74):

$$U_W = \int_0^{D_{\rm Al}} \int_0^L \left\| h_W(z), \frac{k\, Nu(Re_x)}{L} \right\|_{-1} \mathrm{d}x \, \mathrm{d}z \tag{88}$$

The natural convection flow from the vertical faces is upward, perpendicular to the horizontal forced flow; hence, the forced convection U_W and the natural convective conductance $k\, L\, L'\, Nu'/L' = k\, L\, Nu'$ combine as the ℓ^2-norm. The resulting mixed convective conductance is in mild competition with the radiative conductance, $\epsilon_{es}\, \epsilon_{wt}\, h_R\, L\, [D_{\rm Al} + D_{\rm PIR}]$; they combine as the $\ell^{\sqrt{2}}$-norm:

$$\begin{aligned} U_S(u) = {}& 2\, \left\| \epsilon_{es}\, \epsilon_{wt}\, h_R\, L\, [D_{\rm Al} + D_{\rm PIR}],\ \| U_W, k\, L\, Nu' \|_2 \right\|_{\sqrt{2}} \\ &+ 2\, \left\| \epsilon_{es}\, \epsilon_{wt}\, h_R\, L\, [D_{\rm Al} + D_{\rm PIR}],\ k\, L\, Nu' \right\|_{\sqrt{2}} \end{aligned} \tag{89}$$

Each of the four side's natural convective conductance is from the vertical plate formula (Nu') in Jaffer [25], with characteristic-length $L' = D_{\rm Al} + \sqrt{2}\, \varepsilon$, where the metal slab thickness $D_{\rm Al} \approx 19.4$ mm.

Collecting into $U_T(u)$ formula (90) those terms which have a factor of temperature difference $T_P - T_F$, formula (91) is the heat balance equation of the plate during convective cooling:

$$U_T(u) = U_S(u) + \{\overline{h}(u)\, A\} + \epsilon_{rs}\, \epsilon_{wt}\, h_R\, A \tag{90}$$

$$0 = U_T(u)\ [T_P - T_F] + U_I\, [T_P - T_B] + C_{pt}\, \frac{\mathrm{d}T_P}{\mathrm{d}t} \tag{91}$$

Temperatures are functions of time t. Determined experimentally, the temperature group-delay through the 2.54 cm block of insulation between the slab and back sheet is 110 s:

$$T_P(t) = \frac{U_T(u)\, T_F(t) + U_I\, T_B(t - 110\ \mathrm{s}) - C_{pt}\, \mathrm{d}T_P(t)/\mathrm{d}t}{U_T(u) + U_I} \tag{92}$$

To compute Nusselt number $\overline{Nu} = \overline{h}\, L/k$, equation (92) is solved for the $\{\overline{h}(u,t)\, A\}$ term from equation (90).

$$\eta(u,t) = -U_I\ [T_P(t) - T_B(t - 110\ \mathrm{s})] \tag{93}$$

$$\overline{h}(u,t)\, A = \frac{\eta(u,t) - C_{pt}\ [T_P(t) - T_P(t')]\,/[t - t']}{\overline{T_P}(t) - \overline{T_F}(t)} - A\, \epsilon_{rs}\, \epsilon_{wt}\, h_R - U_S(u) \tag{94}$$

where t' is the previous value of t. In the denominator of equation (94), $\overline{T_P}(t)$ and $\overline{T_F}(t)$ are the 11-element cosine averages of plate and fluid temperature (centered at time t).

Following Abernethy, Benedict, and Dowdell [31], the final steps in processing an experiment's data are:

1) Using equation (94), calculate the sensitivities of convected power $\overline{h}\,A\,\Delta T$ per each parameter at its mean value during the measurement interval;
2) multiply each sensitivity by its estimated parameter bias to yield the component uncertainties;
3) calculate the root-sum-squared (RSS) of these uncertainties to yield the RSS measurement uncertainty.

symbol	**nominal**	**sensitivity**	**bias**	**uncertainty**	**component**
T	293K	−0.172%/K	1.0K	0.17%	LM35C temperature sensor
ΔT	10.5K	7.97%/K	0.15K	1.20%	LM35C differential
P	101kPa	0.0007%/Pa	1.5kPa	1.07%	MPXH6115A6U air pressure
u	2.00m/s	35.1%/(m/s)	30mm/s	1.05%	airspeed
u_u	7.50m/s	0.576%/(m/s)	0.20m/s	0.12%	airspeed upper bound
L_w	0.305m	226%/m	500um	0.11%	plate width
ς	6.00mm	5498%/m	200um	1.10%	peak height-of-roughness
D_{Al}	19.4mm	238%/m	500um	0.12%	metal slab thickness
C_{pt}	4.69kJ/K	0.018%/(J/K)	42J/K	0.74%	plate thermal capacity
ϵ_{rs}	0.040	14.4%	0.010	0.14%	rough surface emissivity
ϵ_{wt}	0.900	6.10%	0.050	0.31%	wind-tunnel emissivity
				2.38%	RSS combined uncertainty

Table 13 estimated measurement uncertainties, bi-level 3mm roughness at $Re = 40860$

Table 13 lists the sensitivity, bias, and uncertainty for each component contributing more than 0.1% uncertainty. Because the final convective power measurement is the aggregation of thousands of readings, the variability of dynamic variables do not contribute significantly to the uncertainty. The combined measurement uncertainty including all components is 2.38% at $u = 2.0$ m/s. At $u = 0.25$ m/s ($Re = 5108$), the uncertainty grows to 4.75%, as shown in Table 14.

symbol	**nominal**	**sensitivity**	**bias**	**uncertainty**	**component**
T	293K	0.223%/K	1.0K	0.22%	LM35C temperature sensor
ΔT	10.5K	16.9%/K	0.15K	2.53%	LM35C differential
P	101kPa	0.0008%/Pa	1.5kPa	1.26%	MPXH6115A6U air pressure
u	0.250m/s	270%/(m/s)	3.8mm/s	1.01%	airspeed
L_c	0.305m	259%/m	500um	0.13%	characteristic-length
L_w	0.305m	248%/m	500um	0.12%	plate width
ς	6.00mm	5737%/m	200um	1.15%	peak height-of-roughness
D_{Al}	19.4mm	1892%/m	500um	0.95%	metal slab thickness
D_{PIR}	25.4mm	380%/m	1.0mm	0.38%	insulation thickness
D_g	1.00mm	351%/m	500um	0.18%	air gap
L_m	3.57mm	202%/m	500um	0.10%	side metal strip width
k_{PIR}	$23.0\frac{\mathrm{mW}}{\mathrm{K{\cdot}m}}$	$0.477\%/\frac{\mathrm{mW}}{\mathrm{K{\cdot}m}}$	$1.2\frac{\mathrm{mW}}{\mathrm{K{\cdot}m}}$	0.55%	PIR thermal conductivity
k_{XPS}	$33.0\frac{\mathrm{mW}}{\mathrm{K{\cdot}m}}$	$0.085\%/\frac{\mathrm{mW}}{\mathrm{K{\cdot}m}}$	$1.7\frac{\mathrm{mW}}{\mathrm{K{\cdot}m}}$	0.14%	XPS thermal conductivity
C_{pt}	4.69kJ/K	0.036%/(J/K)	42J/K	1.51%	plate thermal capacity
ϵ_{es}	0.710	56.5%	0.014	0.80%	effective side emissivity
ϵ_{rs}	0.040	114%	0.010	1.14%	rough surface emissivity
ϵ_{wt}	0.900	49.8%	0.050	2.49%	wind-tunnel emissivity
θ	90.0°	0.480%/°	0.50°	0.24%	plate angle
				4.72%	RSS combined uncertainty

Table 14 estimated measurement uncertainties, bi-level 3mm roughness at $Re = 5108$